



BRNO UNIVERSITY OF TECHNOLOGY

VYSOKÉ UČENÍ TECHNICKÉ V BRNĚ

FACULTY OF MECHANICAL ENGINEERING

FAKULTA STROJNÍHO INŽENÝRSTVÍ

INSTITUTE OF MATHEMATICS

ÚSTAV MATEMATIKY

NUMERICAL METHODS OF IMAGE PROCESSING FROM NASA'S SDO SPACE PROBE

NUMERICKÉ METODY ZPRACOVÁNÍ OBRAZŮ Z KOSMICKÉ SONDY NASA SDO

MASTER'S THESIS

DIPLOMOVÁ PRÁCE

AUTHOR

AUTOR PRÁCE

Bc. Tomáš Meduňa

SUPERVISOR

VEDOUCÍ PRÁCE

Mgr. Jana Hoderová, Ph.D.

BRNO 2020

Specification Master's Thesis

Department: Institute of Mathematics
Student: **Bc. Tomáš Meduňa**
Study programme: Applied Sciences in Engineering
Study branch: Mathematical Engineering
Supervisor: **Mgr. Jana Hoderová, Ph.D.**
Academic year: 2019/20

Pursuant to Act no. 111/1998 concerning universities and the BUT study and examination rules, you have been assigned the following topic by the institute director Master's Thesis:

Numerical methods of image processing from NASA's SDO space probe

Concise characteristic of the task:

Image analysis of images taken by the instruments of the spacecraft SDO (Solar Dynamic Observatory, developed at NASA) is significant for monitoring of dynamic processes of the Sun. One of the observed wavelengths is 1600 Å (160 nm) which in the photosphere of the Sun corresponds to C IV emission with continuum and 1700 Å (170 nm) which corresponds to the continuum. Thanks to mathematical methods applied to SDO data, more detailed information about the solar photosphere can be obtained.

Goals Master's Thesis:

The goal of this thesis is the formulation of used mathematical theory and developing of the software for the creation of images of C IV emission.

Recommended bibliography:

PRATT, William K. Digital Image Processing, WILEY 2007, xix +735pp, ISBN-13:978-0471767770, ISBN-10: 0471767778.

DRUCKMÜLLER, Miloslav. A NOISE ADAPTIVE FUZZY EQUALIZATIONMETHOD FOR PROCESSING SOLAR EXTREME ULTRAVIOLET IMAGES.The Astrophysical Journal Supplement Series. 2013, vol. 207, issue 2, s. 25-29. DOI: 10.1088/0067-0049/207/2/25.

DRUCKMÜLLEROVÁ, Hana. Phase-correlation based image registration. Brno, 2010. Diploma thesis, Fakulta strojního inženýrství Vysoké učení technické v Brně. Supervisor: Doc. PaedDr. Dalibor Martišek, Ph.D.

Deadline for submission Master's Thesis is given by the Schedule of the Academic year 2019/20

In Brno,

L. S.

prof. RNDr. Josef Šlapal, CSc.
Director of the Institute

doc. Ing. Jaroslav Katolický, Ph.D.
FME dean

Abstrakt

Tato práce se zabývá zpracováním snímků Slunce pořízených kosmickou sondou SDO na různých vlnových délkách a vizualizací výskytu třikrát ionizovaného uhlíku C IV jejich vhodným složením. V práci jsou uvedeny základní informace o Slunci a jeho atmosféře, dále je shrnuta potřebná teorie a možné postupy vizualizace, které jsou následně vyhodnoceny a porovnány. Součástí je i vytvořený program pro snadnou tvorbu snímků vizualizujících uhlík C IV.

Summary

The thesis deals with processing of images of Sun taken by SDO space probe on different wavelengths. The goal is to visualize appearance of three times ionized carbon C IV by suitable composition of images. Basic facts about Sun and its atmosphere are stated, followed by theory and possible visualization approaches, which are in the end evaluated and compared. Within the thesis is also created software for simple creation of carbon C IV images.

Klíčová slova

Uhlík C IV, Fázová korelace, Fourierova transformace, Registrace obrazu, Solar Dynamics Observatory

Keywords

Carbon C IV, Phase correlation, Fourier transform, Image registration, Solar Dynamics Observatory

MEDUŇA, T. *Numerical methods of image processing from NASA's SDO space probe*. Brno: Brno University of Technology, Faculty of Mechanical Engineering, 2020. 63 p. Supervisor of master's thesis Mgr. Jana Hoderová, Ph.D..

I declare that I have written the master's thesis *Numerical methods of image processing from NASA's SDO space probe* on my own according to advice of my master's thesis supervisor Mgr. Jana Hoderová, Ph.D., and using the sources listed in references.

Tomáš Meduňa

I would like to thank my master's thesis supervisor Mgr. Jana Hoderová, Ph.D. for her guidance and valuable suggestions on improving my thesis.

Tomáš Meduňa

Contents

Introduction	13
1 Astronomical background	15
1.1 Sun	15
1.1.1 Photosphere	16
1.1.2 Chromosphere	16
1.1.3 Transition region	16
1.1.4 Solar corona	16
1.1.5 Sunspots and solar flares	17
1.2 Solar Dynamics Observatory	18
1.2.1 Virtual Solar Observatory	18
2 Mathematical theory	20
2.1 Digital image	20
2.1.1 Flexible Image Transport System	20
2.2 Image interpolation methods	21
2.2.1 Nearest neighbour	22
2.2.2 Bilinear interpolation	22
2.2.3 Biquadratic interpolation	23
2.2.4 Bicubic interpolation	24
2.3 Histogram modification	24
2.3.1 Linear transform	26
2.3.2 Gamma correction	26
2.3.3 Kappa Sigma Clipping	26
2.4 Fourier transform	26
2.4.1 2D Fourier transform	26
2.4.2 Discrete 2D Fourier transform	27
2.4.3 Properties of Fourier transform	28
2.4.4 Convolution	31
2.5 Correlation	32
2.5.1 Complex conjugate functions	32
2.5.2 Phase correlation function	34
2.5.3 Sub-pixel precision phase-correlation	36
2.5.4 Polar coordinates	37
2.5.5 Logarithmic-polar coordinates	37
2.6 Weight functions	38
2.6.1 Window function	38
2.6.2 Low-pass high-pass weight function	39
3 Implementation	41
3.1 Algorithm	41
3.1.1 FITS files download	41
3.1.2 Image preprocessing	41
3.1.3 Image registration	42

3.1.4	Multiplicative function computation	42
3.1.5	Image merging	43
3.1.6	Histogram modification	44
3.1.7	Used libraries	45
3.2	Multiplicative function results	47
3.2.1	Evolution in time	49
3.3	Resulting images and video	51
3.4	Graphical user interface	54
3.4.1	Data Selection tab	55
3.4.2	Histogram Modifications and Preview tab	56
3.4.3	Recommended usage and procedure	57
	Conclusion	58
	Bibiliography	60
	List of abbreviations	62
	List of appendices	63

Introduction

The Sun is the nearest and most inspected star to us. Nowadays we know a lot about the life cycle of stars. Despite vast distances, we can categorize and study them based on their spectra. We can tell how old is the star, what will be its future evolution and how long will it take. However, these changes are mostly identified with precision on hundreds millions of years or rather billions of years.

But we want to understand Sun and its behavior more locally and on much shorter time scales. On such time intervals and such local areas, that we could observe changes in Sun's atmosphere and call it Sun's weather. Nowadays we know that the Sun as a whole has approximately eleven years long period of activity variance. It means there are seasons of a higher rate of sunspots, flares and massive mass ejections, and seasons of lower rates.

Observing those phenomena enables us to study its influence on Earth and also can help us to predict those events in advance and determine the chances of having major impact on humans living on Earth. For example, mass ejections may rapidly influence so-called solar wind, which is a stream of high energy electrically charged particles coming out of the Sun. In the case of strong enough ejection and right direction toward the Earth, the caused solar wind of charged particles can make huge temporal changes in Earth's magnetic field, leading even to collapse of power grids. Being able to predict such events with certain precision ahead, we could simply power off endangered systems to prevent damages.

In fact, the Sun is monitored not only from Earth, but mainly from space by probes. We will focus on *Solar Dynamics Observatory (SDO)* and its *Atmospheric Imaging Assembly (AIA)* aboard. AIA takes images in very narrow bands of spectra, focusing on different parts of Sun's atmosphere. Two wavelengths are relevant for us, the 1600 Å and 1700 Å. On both of them, there is imprinted the overall continuum of the Sun radiation with similar intensity rates, as both wavelengths are relatively close to each other. In 1600 Å images, there is also information involved about the presence of three times ionized carbon C IV, which emerges exclusively during ongoing Sun eruptions. Combining images of both wavelengths captured in the same time, we can extract the information about C IV layout in space and get a specific way of visualizing eruptions.

For those purposes, we will have to register a couple of images. The suitable phase correlation method and required mathematical theory, already studied and described from the theoretical point of view in my bachelor's thesis [20], will be reviewed and extended. We will also study and describe the used image format *Flexible Image Transport System (FITS)* and see, whether we can use stored metadata for image processing somehow. We will also focus on well-known image interpolation methods, their suitability and effects on final results.

A further step, combining images requires compensating the slight difference in continuum first. A suitable function has to be found and applied on one of the images before combination. The thesis will also focus on studying the eventual evolution of such a function in time.

The images of the Sun capture very contrasting areas and require further adjustment for human eye. Therefore we will also have to focus on histogram modifications. Finally, we can make a time sequence of corresponding image couples and create a video capturing carbon C IV emission during an eruption.

For the possibility of easy generation of images and videos of carbon C IV, a software (graphical user interface respectively) with relevant parameters will be designed and created.

1 Astronomical background

1.1 Sun

This section serves as a brief overview of Sun's parameters and is a summarization of information listed in [15], [19] and [26]. The Sun is a G-type star of main-sequence. The radius of the Sun is approximately 695 thousand kilometers, which is more than one hundred times bigger than the radius of Earth. Sun is rotating around its axis, but as its surface is not solid, the rotation period varies according to distance from Sun's equator. The shortest period of about 25 days is on the equator and in direction to poles, the speed decreases and the period gets up to 34 days [15].

The Sun's interior composes of individual layers, called in order as *the core*, *radiative zone* and *convective zone* depicted in the figure 1.1. The temperature of Sun's core is estimated to be 15 million Kelvins, decreasing towards the surface. In the interior, the thermonuclear reaction takes place and produces radiation, which is slowly converging by reemissions to the surface.

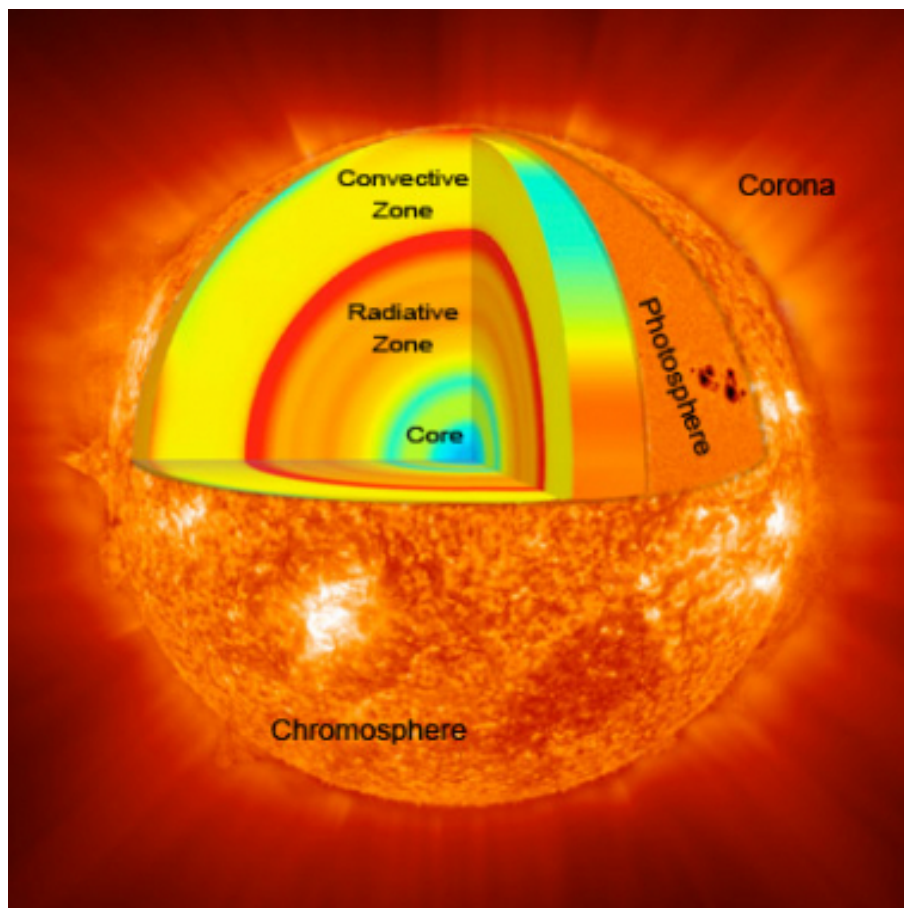


Figure 1.1: Sun's structure ([28]).

We distinguish three main layers of Sun's atmosphere called the *photosphere*, *chromosphere* and *solar corona* which we will now describe in more details.

1.1.1 Photosphere

By photosphere we call roughly 400 kilometers thick upper layer of the convective zone, where Sun becomes opaque, i.e. it is the deepest layer, we can observe. The photosphere is also layer up to which we measure the Sun's radius. The temperature here attains between 4500 and 6000 Kelvins. "The structure of photosphere, called *granulation*, resembles grains of rice spilled on a dark tablecloth or a pot of boiling oatmeal." [19] as can be seen in the figure 1.2. The granules have typically 700 to 1000 kilometers in diameter. On granule's surface, the matter is rising while falling down again into the interior on its edges. Because of the temperature, the density is quite small - about one thousandth of Earth's atmosphere density at sea level, whilst the pressure is one tenth of that one on Earth.

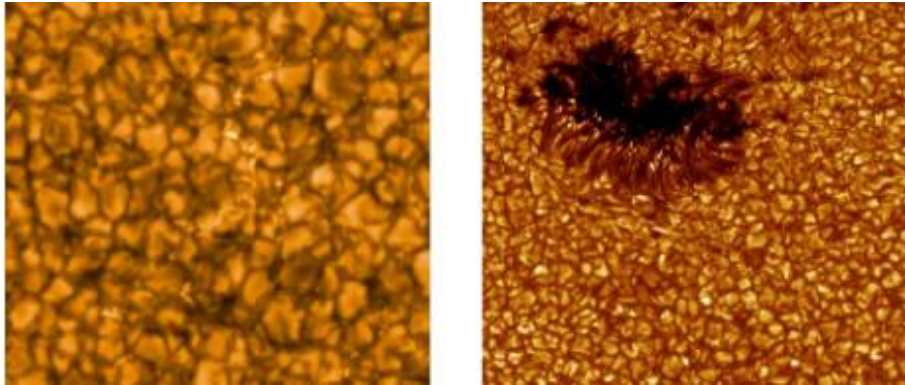


Figure 1.2: Granulation pattern ([19]).

1.1.2 Chromosphere

Another layer above is chromosphere, which is difficult to observe due to the fact, that it is transparent to most of the visible radiation from the photosphere and on its own emits very little amount of light. For a long time, it was possible to observe the chromosphere only during the solar eclipse. It is about 2000 to 3000 kilometers thick and its spectrum contains most of Sun's bright emission lines caused by hot excited gases which emits light at discrete wavelengths. The average temperature is 10000 Kelvins.

1.1.3 Transition region

The region between the chromosphere and solar corona is called transition region. Here, the magnetic force starts to dominate over gravity. It is only a few tens of kilometers wide but the temperature rises with the distance very rapidly to about million Kelvins (see the figure 1.3). Spectral lines of transition region are mostly absorption ones. The transition region is one of the least understood part of Sun's atmosphere, as it is difficult to simulate conditions there.

1.1.4 Solar corona

The upper layer of Sun's atmosphere is solar corona consisting of very hot gases escaping from Sun's photosphere. It is approximately two times brighter than the full moon and the shape is very irregular. It may be millions of kilometers wide to outer space but there

are also regions where there is almost no solar corona observed, such as region called *coronal hole* on the south pole. The temperature is from 1 to 6 million Kelvins but the matter is very sparse. In the certain distance, the density becomes so low, that the probability of one particle hitting another is extremely small and therefore they become a sort of "frozen" in their excited state.

1.1.5 Sunspots and solar flares

Sun's surface consists of electrically charged gases constantly changing their position. They are generating huge magnetic forces forming the Sun's magnetic field. The rate of changes in the magnetic field varies over approximately eleven years long period of solar activity.

Sunspots are cooler parts of Sun's surface with the very strong local magnetic field not allowing some of the heat from Sun to reach that particular surface region. The higher number of sunspots in principal means higher Sun activity.

The magnetic field near sunspots is often complicated and changes over time continuously. From time to time, the induction lines cross each other and so-called magnetic field reorganization may occur, i.e. some of the magnetic induction lines merge, simplifying the magnetic field and decreasing its energy. Redundant energy is often released in a form of intense radiation to outer space called a solar flare. Occasionally, when the magnetic reorganization is large or sudden, solar flares can be accompanied by huge bubbles of radiation and particles exploding into space at high speed. This effect is called a coronal mass ejection.

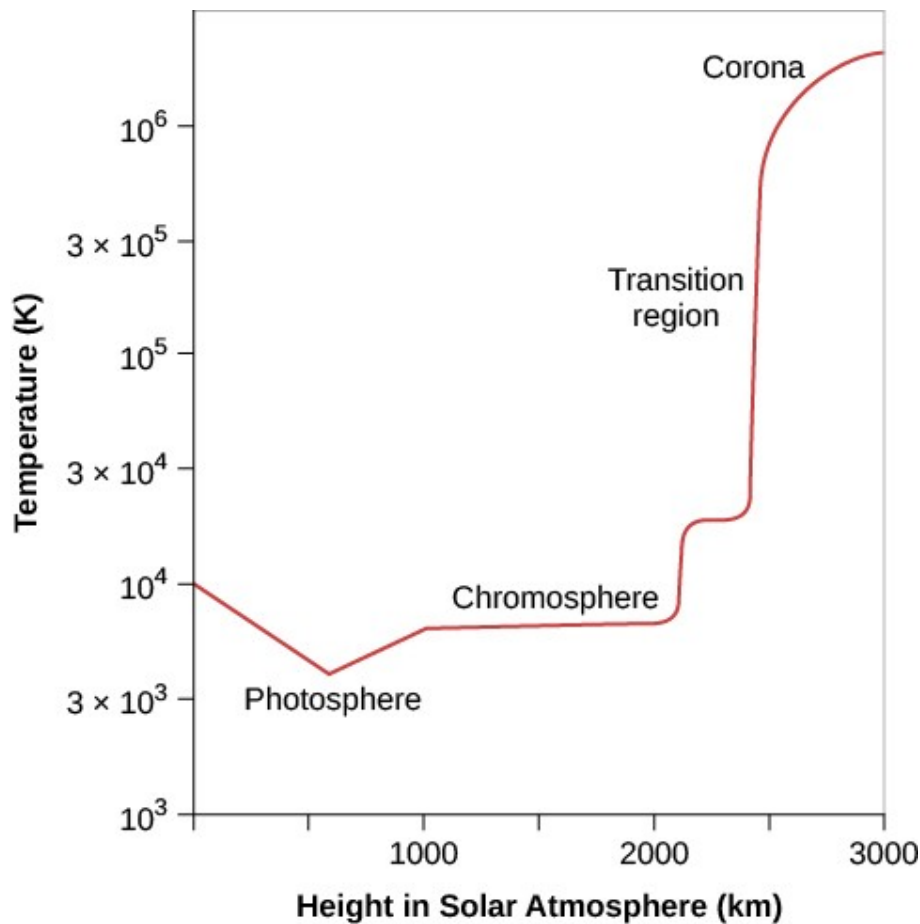


Figure 1.3: Temperature in the solar atmosphere ([19]).

1.2 Solar Dynamics Observatory

The Solar Dynamics Observatory (SDO) is a space probe of NASA studying Sun's activity. SDO was launched in 2010 in order to catch sunspot and solar activity during its predicted peak in 2013 as part of Sun's 11-year cycle. The probe continuously records high-definition views of the Sun's atmosphere from a geosynchronous orbit, where an orbital period of satellite matches the period of Earth's rotation on its axis. The probe consists of several instruments, namely Atmospheric Imaging Assembly (AIA), Helioseismic Magnetic Imager (HMI) and Extreme Ultraviolet Experiment (EVE) as it is depicted in the figure 1.4.

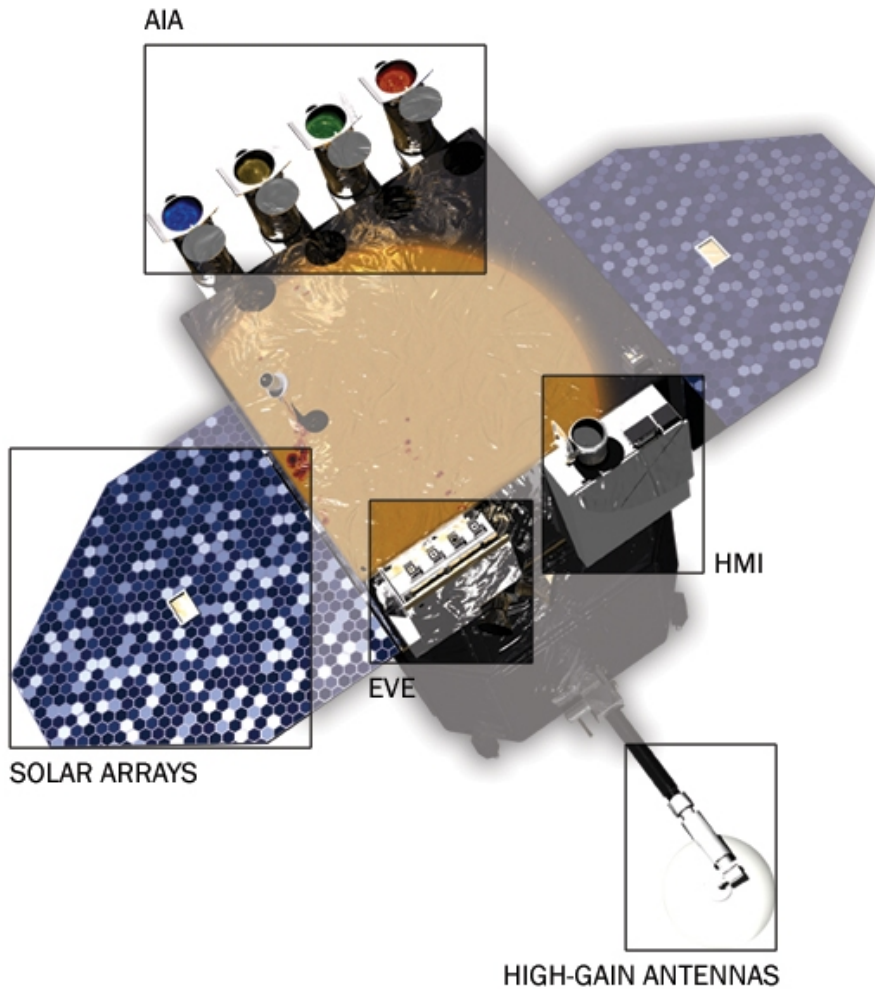


Figure 1.4: Solar Dynamics Observatory and its instruments ([12]).

Detectors are equipped with several narrow-wavelength filters based on one or two types of ions and their spectral emission lines. According to [10] each wavelength was chosen to highlight a particular part of Sun's atmosphere, from the solar surface to the upper reaches of Sun's corona and it is depicted in the table 1.1. Symbol \AA denotes a unit of wavelength called *angstrom* and it holds $1 \text{\AA} = 10^{-10} \text{ m} = 0.1 \text{ nm}$.

1.2.1 Virtual Solar Observatory

The Virtual Solar Observatory (VSO) is a tool providing access to most of NASA mission's data, such as images from space probes. Being able to specify for example time, instrument

Table 1.1: The primary ions observed by AIA ([18]).

Channel	Primary ion(s)	Region of atmosphere	Char. log(T)
4500 Å	continuum	photosphere	3.7
1700 Å	continuum	temperature minimum, photosphere	3.7
304 Å	He II	chromosphere, transition region	4.7
1600 Å	C IV + cont	transition region, upper photosphere	5.0
171 Å	Fe IX	quiet corona, upper transition region	5.8
193 Å	Fe XII, XXIV	corona and hot flare plasma	6.2, 7.3
211 Å	Fe XIV	active-region corona	6.3
335 Å	Fe XVI	active-region corona	6.4
94 Å	Fe XVIII	flaring corona	6.8
131 Å	Fe VIII, XXI	transition region, flaring corona	5.6, 7.0

and spectral range, we are able to obtain only data we are interested in. Individual images are stored in `.fits` format which is described further in chapter 2. The Virtual Solar Observatory is accessible at <https://sdac.virtualsolar.org/cgi/search>.

In order to study the occurrence of three times ionized atoms of carbon C IV, we are focusing on wavelengths 1600 Å and 1700 Å, both capturing Sun’s photosphere. The shorter wavelength 1600 Å captures continuum which is the visible part of Sun’s spectrum with a temperature 5000 K and occurrence of carbon C IV with temperature around 10000 K. On the longer wavelength 1700 Å, only the continuum is captured. Both wavelengths are quite close to each other, hence the continuum should have similar representation in both of them. Therefore by combining both images we should be able to separate information about C IV particles. C IV is present in the upper photosphere and in the transition region, where the temperature rapidly rises. It is produced largely during stronger solar flares and mass coronal ejections. On both wavelength images are regularly taken each 24 seconds.

2 Mathematical theory

2.1 Digital image

Definition 2.1 (Digital gray-scale image) Let $R = \{0, 1, \dots, M - 1\} \times \{0, 1, \dots, N - 1\}$, $M, N \in \mathbb{N}$ and let $W = \{0, 1, \dots, w - 1\}$, $w \in \mathbb{N}$. The function

$$f : R \rightarrow W$$

is called a *digital gray-scale image* or *image* [6], [20], M is called *image width* and N the *image height*. Elements of R are called *pixels*, value of function f in pixel (x, y) is called the *pixel value*. The natural number w determines the *dynamic range*. We say that the *dynamic range* is *n-bits image* if $w = 2^n$, where $n \in \mathbb{N}$.

Definition 2.2 (Digital color image) A *digital color image* is a triple of digital gray-scale images (r, g, b) which are called (in order) the *red*, *green* and *blue color channel*.

Remark 2.1 Digital image is a discrete function of two variables on a restricted area represented by a chart (or matrix) of function values.

Remark 2.2 In a visualisation of a grey-scale image, the black color corresponds to a minimum pixel value and white color to a maximum.

2.1.1 Flexible Image Transport System

Although being originally designed for transporting images on magnetic tape, the Flexible Image Transport System (FITS) is nowadays standard format used in astronomy to store and share data [9].

FITS is composed of tuples called *Header/Data Units (HDUs)*. Every HDU clearly comprise of the *Header Unit* followed by an optional *Data Unit*. Both of them are a multiple of 2880 bytes long. If needed the rest of bytes up to a multiple is filled with blank values in the Header and NULLs in data units respectively.

The first HDU called *Primary HDU* or *Primary Array* may contain 1 to 999 dimensional array of integers or floating point numbers. If there are any other HDUs, we call them as *extensions*. Nowadays there are three types of standard extensions:

- IMAGE - 0 to 999 dimensional array of pixels
- TABLE - data in ASCII format
- BINTABLE - data in binary representation

Each header is a sequence of 80 keyword records restricted to ASCII characters. Record begins with 8 characters long keyword containing only uppercase English alphabet letters, digits, hyphen and underscore character, usually continues by equal sign and numeric value (integer, floating point number, complex number or pair of numbers), character string (enclosed in single quotes), or a Boolean value (letter T or F).

Some relevant header records and their meaning are listed in the table 2.1. The image pixels are indexed from 1, we have to take it into account, especially when using values *CRPIX1* and *CRPIX2*. The header ends with keyword *END* with a blank value.

Table 2.1: Important FITS header records ([9], [27]).

Keyword	Meaning
BITPIX	number of bits per data pixel
NAXIS	number of data axes
NAXIS1	length of data axis 1
NAXIS2	length of data axis 2
DATE	date of data creation (UTC)
WAVELNTH	wavelength of spectrum observed
DATAMIN	minimum pixel value
DATAMAX	maximum pixel value
DATAMED	median of pixel values
DATAMEAN	mean of pixel values
CRPIX1	location of reference point on axis 1
CRPIX2	location of reference point on axis 2
CROTA2	bulk rotation of image plane
R_SUN	radius of Sun in pixels

2.2 Image interpolation methods

Several methods for interpolation of pixel values during the application of image transformation will be introduced now. In the end, we compare all mentioned methods in the sense of computational cost and quality of output image. All methods search for transformed image pixels in the domain image and get the value of result pixels using corresponding weight function often called convolution kernel, denoted by h . We will use discrete convolution to compute transformed image pixel values (see definition 2.18). As all the kernel functions h are usually rotationally symmetric, we will prescribe them and illustrate their principle on functions of single variable x .

In order to be suitable for interpolation, the kernel must satisfy the following conditions:

1. $h(0) = 1$.
2. $h(x) = 0$ for $|x| = 1, 2, \dots$
3. For any displacement d , such that $0 \leq d < 1$, the sum of h of all value $x \in \mathbb{Z}$ is equal to 1, i.e.

$$\sum_{x \in \mathbb{Z}} h(x + d) = 1.$$

In other words, the kernel function has to be designed in such a way, that represents a weight function for lattice of image pixels regardless of the reference position x_0 with respect to the lattice.

Also by δ we denote the size of the neighbourhood, which is taken into account in particular interpolation method kernel, giving us notation of kernel function as $h_\delta(x)$.

2.2.1 Nearest neighbour

The easiest and most intuitive method called *nearest neighbour* simply takes each pixel of transformed image and looks for its representative position in the domain. As the domain is also a discrete set of pixels, it chooses the closest pixel and copies its value.

$$h_1(x) = \begin{cases} 1 & \text{if } 0 \leq |x| < 0.5, \\ 0 & \text{otherwise.} \end{cases} \quad (2.1)$$

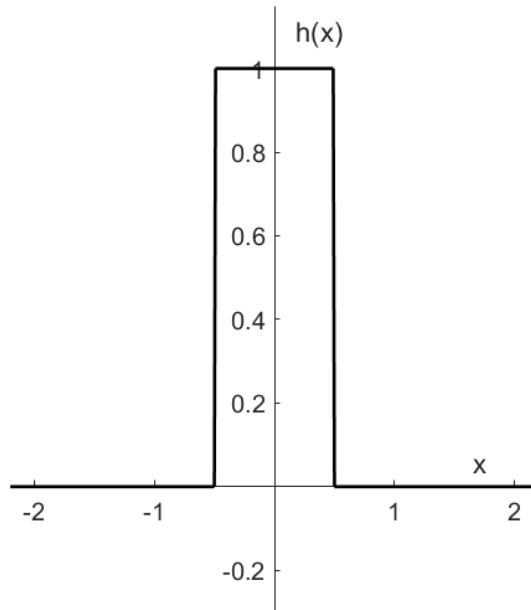


Figure 2.1: Nearest neighbour interpolation kernel.

This process often results in a spatial offset error getting up to $\frac{1}{\sqrt{2}}$ pixel units, accompanied by strong aliasing and blurring. For obvious reasons, the procedure is not suitable for images designed for further study. The nearest neighbour method still takes place in situations, when a fast transformation is required regardless of the quality losses, such as magnifier tools. But we will no longer take this method into account.

2.2.2 Bilinear interpolation

Bilinear interpolation consists of two sequential linear interpolations. When choosing kernel of size $\delta = 2$, for each resulting pixel, four pixels surrounding the reference domain positions are selected. For each pair of pixels, an interpolated value is computed according to a distance on the selected axis. Finally the linear value of those two interpolated values is computed according to a distance on the other axis.

Even though both interpolations are linear, the reconstructed surface surrounded by those four pixels obtained by bilinear interpolation is generally nonlinear.

$$h_2(x) = \begin{cases} 1 - |x| & \text{if } 0 \leq |x| < 1, \\ 0 & \text{otherwise.} \end{cases} \quad (2.2)$$

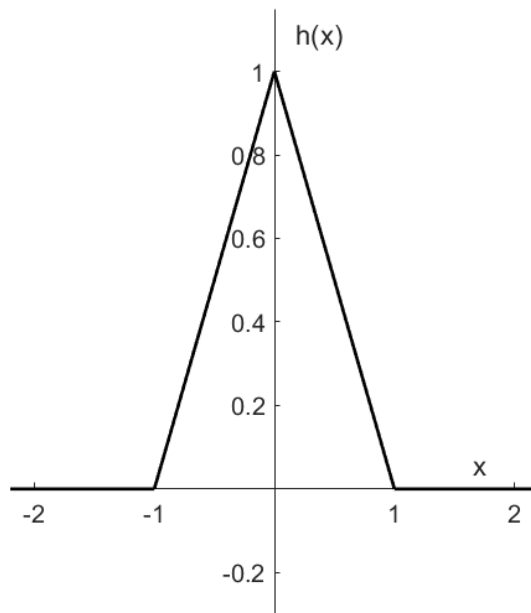


Figure 2.2: Linear interpolation kernel.

In comparison with the nearest neighbour, the bilinear interpolation has much weaker aliasing effect, but low frequencies are still aliased. In addition, the higher frequencies are being attenuated, which results in lower image contrast.

2.2.3 Biquadratic interpolation

Biquadratic interpolation takes into account more surrounding pixels and interpolates them by parabolic function.

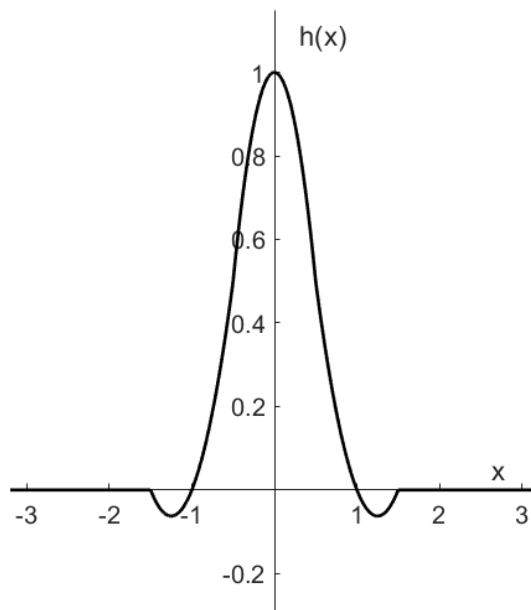


Figure 2.3: Quadratic interpolation kernel with parameter $a = 1$.

$$h_3(x) = \begin{cases} -2ax^2 & + \frac{1}{2}(a+1) & \text{if } 0 \leq |x| < \frac{1}{2}, \\ ax^2 & - (2a + \frac{1}{2})|x| & + \frac{3}{4}(a+1) & \text{if } \frac{1}{2} \leq |x| < \frac{3}{2}, \\ 0 & & & \text{otherwise.} \end{cases} \quad (2.3)$$

Biquadratic interpolation also attenuates high spatial frequencies [17].

2.2.4 Bicubic interpolation

Bicubic polynomials are widely used thanks to their ability to fit C^2 continuous functions. We will focus on kernels of size $\delta \in \{4, 6, 8\}$. Their equations are given below.

Bicubic interpolation with kernel of size $\delta = 4$ has one degree of freedom given in the parameter a . According to [17], several values were found to be convenient, for example $a = -1.3$ or $a = -0.5$. Given $a = -0.5$, the bicubic interpolation can reconstruct an arbitrary second degree polynomial. It was derived to be an optimal value of a for image independent case.

$$h_4(x) = \begin{cases} (a+2)|x|^3 & -(a+3)x^2 & +1 & \text{if } 0 \leq |x| < 1, \\ a|x|^3 & -5ax^2 & +8a|x| & -4a & \text{if } 1 \leq |x| < 2, \\ 0 & & & & \text{otherwise.} \end{cases} \quad (2.4)$$

$$h_6(x) = \begin{cases} \frac{6}{5}|x|^3 & -\frac{11}{5}x^2 & +1 & \text{if } 0 \leq |x| < 1, \\ -\frac{3}{5}|x|^3 & +\frac{16}{5}x^2 & -\frac{27}{5}|x| & +\frac{14}{5} & \text{if } 1 \leq |x| < 2, \\ \frac{1}{5}|x|^3 & -\frac{8}{5}x^2 & +\frac{21}{5}|x| & -\frac{18}{5} & \text{if } 2 \leq |x| < 3, \\ 0 & & & & \text{otherwise.} \end{cases} \quad (2.5)$$

$$h_8(x) = \begin{cases} \frac{67}{56}|x|^3 & -\frac{123}{56}x^2 & +1 & \text{if } 0 \leq |x| < 1, \\ -\frac{33}{56}|x|^3 & +\frac{177}{56}x^2 & -\frac{75}{14}|x| & +\frac{39}{14} & \text{if } 1 \leq |x| < 2, \\ \frac{9}{56}|x|^3 & -\frac{75}{56}x^2 & +\frac{51}{14}|x| & -\frac{45}{14} & \text{if } 2 \leq |x| < 3, \\ -\frac{3}{56}|x|^3 & +\frac{33}{56}x^2 & -\frac{15}{7}|x| & +\frac{18}{7} & \text{if } 3 \leq |x| < 4, \\ 0 & & & & \text{otherwise.} \end{cases} \quad (2.6)$$

2.3 Histogram modification

Usually, when observing the image histogram, we might come to a decision, that a certain histogram transformation is needed. For example, when SDO takes images of the Sun on wavelength 1600 Å during an intensive solar flare, most of the image pixel values are going to be very low, considering the provided dynamic range. Only a few pixels capturing the Sun's part with solar flare are going to be very high and close to the top of dynamic range. The resulting image is therefore very contrast from the point of view of comparing the solar flare region and the rest of the Sun. But solar flare takes only a fraction of an image. The rest of the Sun will be very monotonous and low contrast. This can be fixed by suitable histogram modification.

We will introduce two basic examples of histogram modification with a global approach. With respect to the histogram of an image, suitable parameters of transforming function

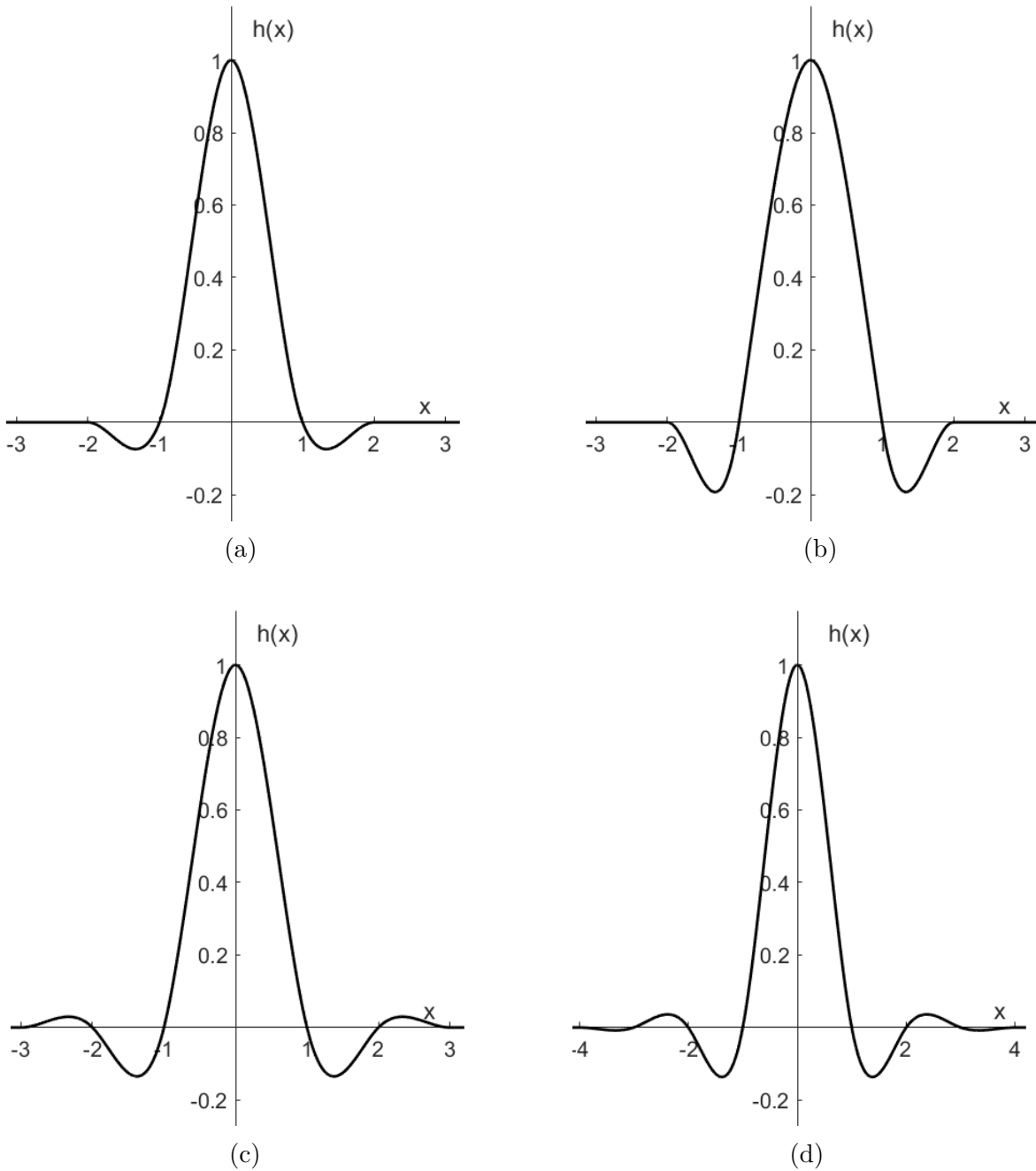


Figure 2.4: Cubic kernel functions.

- (a) Cubic kernel h_4 with parameter $a = -0.5$.
- (b) Cubic kernel h_4 with parameter $a = -1.3$.
- (c) Cubic kernel h_6 .
- (d) Cubic kernel h_8 .

are derived. Then on every pixel in the image, exactly the same transformation function is applied. Mostly we want to apply such a transformation when not all the dynamic range is used or because the image is either too dark or bright. Therefore we search for minimum pixel value a_0 and maximum a_1 . Often quantiles $Q_{0,01}$ and $Q_{0,99}$ are used as values a_0 and a_1 respectively.

2.3.1 Linear transform

Definition 2.3 (Linear transform) Given the image f with minimum and maximum pixel value a_0 and a_1 respectively, and original pixel value v_{in} , the new pixel value v_{out} after *linear transform* is defined by

$$v_{out} = b_0 + (b_1 - b_0) \cdot \left(\frac{v_{in} - a_0}{a_1 - a_0} \right),$$

where constants b_0 and b_1 respectively are minimum and maximum pixel values of output image.

2.3.2 Gamma correction

Definition 2.4 (Gamma correction) Given the image f with minimum and maximum pixel value a_0 and a_1 respectively, and original pixel value v_{in} , the new pixel value v_{out} after *gamma correction* [5], [25] with parameter γ is defined by

$$v_{out} = b_0 + (b_1 - b_0) \cdot \left(\frac{v_{in} - a_0}{a_1 - a_0} \right)^{\gamma^{-1}},$$

where constants b_0 and b_1 respectively are minimum and maximum pixel values of output image.

Remark 2.3 The standard γ value for a PC computer display is $\gamma = 2.2$ [5].

2.3.3 Kappa Sigma Clipping

The Kappa Sigma Clipping method [7] is widely used for thresholding images mostly composed of background pixels. For instance, given a set of images, we compute the median m of all pixel values. Then the standard deviation σ of pixel values is calculated. We remove all pixel values outside the interval $\langle m - l \cdot \sigma, m + l \cdot \sigma \rangle$, where the constant l is usually substituted by number 2. Steps can be iterated multiple times. Finally, the mean or median of remaining values is computed.

2.4 Fourier transform

We have been using spatial representation for describing images so far. Now we introduce another approach, namely Fourier (or frequency) domain. Instead of using spatial coordinates x and y , we express the image as a function of spatial frequencies ξ and η . An instrument for the transition from spatial representation to frequency one is called Fourier transform.

2.4.1 2D Fourier transform

Firstly we need to determine the space of all admissible functions for which the Fourier transform exists.

Definition 2.5 ($\mathcal{L}(\mathbb{R}^2)$) Let $\mathcal{L}(\mathbb{R}^2)$ [8], [20] be the space of all functions $\mathbb{R}^2 \rightarrow \mathbb{C}$, such that

$$\iint_{\mathbb{R}^2} |f(x, y)| dx dy$$

exists and is finite.

Definition 2.6 (Fourier transform of functions in $\mathcal{L}(\mathbb{R}^2)$) Let $f \in \mathcal{L}(\mathbb{R}^2)$. The *Fourier transform* (FT) [1], [20] of function f is a function $\mathcal{F}\{f\} = F : \mathbb{R}^2 \rightarrow \mathbb{C}$ defined by

$$F(\xi, \eta) = \int_{-\infty}^{\infty} \int_{-\infty}^{\infty} f(x, y) e^{-i(x\xi + y\eta)} dx dy.$$

Remark 2.4 The function F is also called the *Fourier spectrum* or *Fourier image* of the function f .

Definition 2.7 (Inverse Fourier transform of functions in $\mathcal{L}(\mathbb{R}^2)$) Let $G \in \mathcal{L}(\mathbb{R}^2)$. The *inverse Fourier transform* (IFT) [1], [20] of function G is a function $\mathcal{F}^{-1}\{G\} = g : \mathbb{R}^2 \rightarrow \mathbb{C}$ defined by

$$g(x, y) = \frac{1}{4\pi^2} \int_{-\infty}^{\infty} \int_{-\infty}^{\infty} G(\xi, \eta) e^{i(x\xi + y\eta)} dx dy.$$

Remark 2.5 Fourier spectrum F is, in general, a complex function and includes both dependences of intensity and initial phase on frequency.

Definition 2.8 (Amplitude and phase spectrum) Let $f \in \mathcal{L}(\mathbb{R}^2)$ and F be corresponding Fourier spectrum. The function $A : \mathbb{R}^2 \rightarrow \mathbb{R}_0^+$ defined by

$$A(\xi, \eta) = |F(\xi, \eta)| = \sqrt{[\operatorname{Re}(F(\xi, \eta))]^2 + [\operatorname{Im}(F(\xi, \eta))]^2}$$

is called *amplitude spectrum* [29], [8], [20] of function f and function $\Phi(\xi, \eta) : \mathbb{R}^2 \rightarrow \langle 0, 2\pi \rangle$ defined by

$$\operatorname{Re}(F(\xi, \eta)) = A(\xi, \eta) \cos \Phi(\xi, \eta),$$

$$\operatorname{Im}(F(\xi, \eta)) = A(\xi, \eta) \sin \Phi(\xi, \eta)$$

is called *phase spectrum* [8], [20] of function f .

If $A(\xi, \eta) = 0$, for some (ξ, η) we define $\Phi(\xi, \eta) = 0$.

2.4.2 Discrete 2D Fourier transform

Definition 2.9 (Discrete Fourier transform) Let f be a function $\{0, 1, \dots, N-1\} \times \{0, 1, \dots, N-1\} = \{0, 1, \dots, N-1\}^2 \rightarrow \mathbb{C}$, $N \in \mathbb{N}$. The *discrete Fourier transform* (DFT) [1] of function f is a function $\mathcal{D}\{f\} = F : \{0, 1, \dots, N-1\}^2 \rightarrow \mathbb{C}$ defined by

$$F(\xi, \eta) = \sum_{x=0}^{N-1} \sum_{y=0}^{N-1} f(x, y) e^{-\frac{2\pi i}{N}(x\xi + y\eta)}.$$

Definition 2.10 (Inverse discrete Fourier transform) Let f be a function $\{0, 1, \dots, N-1\}^2 \rightarrow \mathbb{C}$, $N \in \mathbb{N}$ and let F be its discrete Fourier transform. The *inverse discrete Fourier transform* (IDFT) [1] of function F is a function $\mathcal{D}^{-1}\{F\} = \{0, 1, \dots, N-1\}^2 \rightarrow \mathbb{C}$ defined by

$$\mathcal{D}^{-1}\{F\}(x, y) = \frac{1}{N^2} \sum_{\xi=0}^{N-1} \sum_{\eta=0}^{N-1} F(\xi, \eta) e^{\frac{2\pi i}{N}(x\xi + y\eta)}.$$

Considering an image of dimensions $N \times N$, the number of operations of Discrete Fourier transform is $O(N^2)$. More efficient algorithms were developed in order to reduce the number of operations. For example *Cooley-Tukey* algorithm, which is recursively dividing DFT problem to two smaller DFT problems, reaches $O(N \log_2 N)$ number of operations [13].

2.4.3 Properties of Fourier transform

Let us now remind some important properties of Fourier transform from [8]. There are examples of image function transformation and its impact on Fourier image in the table 2.2 below. Introduced properties are formulated for continuous functions. However similar analogous statements hold also for discrete functions.

Remark 2.6 Fourier image is uniquely determined by its spatial function (up to sets of zero measure) [1] and vice versa. Therefore we can introduce a concept of *Fourier pair* in following table.

Fourier pair	$f(x, y)$	$F(\xi, \eta)$
Translation	$f(x - x_0, y - y_0)$	$F(\xi, \eta)e^{-i(\xi x_0 + \eta y_0)}$
Scale change	$f(\alpha x, \alpha y)$	$\frac{1}{\alpha^2} F\left(\frac{\xi}{\alpha}, \frac{\eta}{\alpha}\right)$
Rotation	$f(x \cos \theta - y \sin \theta, x \sin \theta + y \cos \theta)$	$F(\xi \cos \theta - \eta \sin \theta, \xi \sin \theta + \eta \cos \theta)$

Table 2.2: Fundamental properties of Fourier transform.

Theorem 2.11 (Shift theorem) [8], [20] Let function $f_1 \in \mathcal{L}(\mathbb{R}^2)$ and F_1 be its Fourier spectrum, further let us define function f_2 by

$$f_2(x, y) = f_1(x - x_0, y - y_0),$$

where $x_0, y_0 \in \mathbb{R}$ are given constants. Let F_2 be Fourier spectrum of function f_2 . Then

$$F_2(\xi, \eta) = F_1(\xi, \eta)e^{-i(\xi x_0 + \eta y_0)},$$

$$A_2(\xi, \eta) = A_1(\xi, \eta).$$

Proof. The proof is taken from [8].

$$\begin{aligned}
F_2(\xi, \eta) &= \int_{-\infty}^{\infty} \int_{-\infty}^{\infty} f_1(x - x_0, y - y_0) e^{-i(x\xi + y\eta)} dx dy = \\
&= \left| \begin{array}{l} s = x - x_0 \quad x = s + x_0 \quad dx = ds \\ t = y - y_0 \quad y = t + y_0 \quad dy = dt \end{array} \right| = \\
&= \int_{-\infty}^{\infty} \int_{-\infty}^{\infty} f_1(s, t) e^{-i[\xi(s+x_0) + \eta(t+y_0)]} ds dt = \\
&= \int_{-\infty}^{\infty} \int_{-\infty}^{\infty} f_1(s, t) e^{-i(\xi s + \xi x_0 + \eta t + \eta y_0)} dx dy = \\
&= \int_{-\infty}^{\infty} \int_{-\infty}^{\infty} f_1(s, t) e^{-i(\xi s + \eta t)} e^{-i(\xi x_0 + \eta y_0)} ds dt = F_1(\xi, \eta) e^{-i(\xi x_0 + \eta y_0)}.
\end{aligned}$$

Let A_1, A_2 be amplitude spectra of function f_1, f_2 . Then

$$A_2(\xi, \eta) = |F_1(\xi, \eta) e^{-i(\xi x_0 + \eta y_0)}| = |F_1(\xi, \eta)| \cdot |e^{-i(\xi x_0 + \eta y_0)}| = A_1(\xi, \eta) \cdot 1 = A_1(\xi, \eta).$$

□

Theorem 2.12 (Scale-change theorem) [8], [20] Let $f_1 \in \mathcal{L}(\mathbb{R}^2)$ and let F_1 be its Fourier image, further let us define function f_2 by

$$f_2(x, y) = f_1(\alpha x, \alpha y),$$

where $\alpha \in \mathbb{R}^+$ is a given constant. Let F_2 be the Fourier spectrum of function f_2 and let A_1, A_2 be amplitude spectra of functions f_1, f_2 . Then

$$\begin{aligned}
F_2(\xi, \eta) &= \frac{1}{\alpha^2} F_1\left(\frac{\xi}{\alpha}, \frac{\eta}{\alpha}\right), \\
A_2(\xi, \eta) &= \frac{1}{\alpha^2} A_1\left(\frac{\xi}{\alpha}, \frac{\eta}{\alpha}\right).
\end{aligned}$$

Proof. The proof is taken from [8].

$$\begin{aligned}
F_2(\xi, \eta) &= \int_{-\infty}^{\infty} \int_{-\infty}^{\infty} f_2(x, y) e^{-i(x\xi + y\eta)} dx dy = \int_{-\infty}^{\infty} \int_{-\infty}^{\infty} f_1(\alpha x, \alpha y) e^{-i(x\xi + y\eta)} dx dy = \\
&= \left| \begin{array}{l} s = \alpha x \quad x = \frac{s}{\alpha} \quad dx = \frac{ds}{\alpha} \\ t = \alpha y \quad y = \frac{t}{\alpha} \quad dy = \frac{dt}{\alpha} \end{array} \right| = \\
&= \frac{1}{\alpha^2} \int_{-\infty}^{\infty} \int_{-\infty}^{\infty} f_2(s, t) e^{-i(\frac{s}{\alpha}\xi + \frac{t}{\alpha}\eta)} ds dt = \frac{1}{\alpha^2} F_1\left(\frac{\xi}{\alpha}, \frac{\eta}{\alpha}\right), \\
A_2(\xi, \eta) &= |F_2(\xi, \eta)| = \frac{1}{\alpha^2} \left| F_1\left(\frac{\xi}{\alpha}, \frac{\eta}{\alpha}\right) \right| = \frac{1}{\alpha^2} A_1\left(\frac{\xi}{\alpha}, \frac{\eta}{\alpha}\right).
\end{aligned}$$

□

Theorem 2.13 (Rotation theorem) [8], [20] Let $f_1 \in \mathcal{L}(\mathbb{R}^2)$ and let F_1 be its Fourier image, further let us define function f_2 by

$$f_2(x, y) = f_1(x \cos \theta - y \sin \theta, x \sin \theta + y \cos \theta),$$

where $\theta \in \langle 0, 2\pi \rangle$ is a given constant. Let F_2 be the Fourier spectrum of function f_2 and let A_1, A_2 be amplitude spectra of functions f_1, f_2 . Then

$$\begin{aligned} F_2(\xi, \eta) &= F_1(\xi \cos \theta - \eta \sin \theta, \xi \sin \theta + \eta \cos \theta), \\ A_2(\xi, \eta) &= A_1(\xi \cos \theta - \eta \sin \theta, \xi \sin \theta + \eta \cos \theta). \end{aligned}$$

Proof. The proof is taken from [8].

$$\begin{aligned} F_2(\xi, \eta) &= \int_{-\infty}^{\infty} \int_{-\infty}^{\infty} f_2(x, y) e^{-i(x\xi + y\eta)} dx dy = \\ &= \int_{-\infty}^{\infty} \int_{-\infty}^{\infty} f_1(x \cos \theta - y \sin \theta, x \sin \theta + y \cos \theta) e^{-i(x\xi + y\eta)} dx dy = \\ &= \left| \begin{array}{cc} s = x \cos \theta - y \sin \theta & x = s \cos \theta + t \sin \theta \\ t = x \sin \theta + y \cos \theta & y = -s \sin \theta + t \cos \theta \end{array} \right| J = \det \begin{pmatrix} \cos \theta & \sin \theta \\ -\sin \theta & \cos \theta \end{pmatrix} \\ &= \left| \det \begin{pmatrix} \cos \theta & \sin \theta \\ -\sin \theta & \cos \theta \end{pmatrix} \right| \int_{-\infty}^{\infty} \int_{-\infty}^{\infty} f_1(s, t) e^{-i[(s \cos \theta + t \sin \theta)\xi + (-s \sin \theta + t \cos \theta)\eta]} ds dt = \\ &= 1 \cdot \int_{-\infty}^{\infty} \int_{-\infty}^{\infty} f_1(s, t) e^{-i[s(\xi \cos \theta - \eta \sin \theta) + t(\xi \sin \theta + \eta \cos \theta)]} ds dt = \\ &= F_1(\xi \cos \theta - \eta \sin \theta, \xi \sin \theta + \eta \cos \theta). \end{aligned}$$

□

Theorem 2.14 (Similarity theorem) [8], [20] Let function $f_1 \in \mathcal{L}(\mathbb{R}^2)$ and let F_1 be its Fourier spectrum, further let us define function f_2 by

$$f_2(x, y) = f_1(\alpha x \cos \theta - \alpha y \sin \theta - x_0, \alpha x \sin \theta + \alpha y \cos \theta),$$

where $\theta \in \langle 0, 2\pi \rangle$, $\alpha \in \mathbb{R}^+$ and $x_0, y_0 \in \mathbb{R}$ are given constants. Let function F_2 be the Fourier spectrum of function f_2 and let functions A_1, A_2 be amplitude spectra of functions f_1, f_2 . Then

$$\begin{aligned} F_2(\xi, \eta) &= \frac{1}{\alpha^2} e^{-i(\xi x_0 + \eta y_0)} F_1 \left(\frac{\xi}{\alpha} \cos \theta - \frac{\eta}{\alpha} \sin \theta, \frac{\xi}{\alpha} \sin \theta + \frac{\eta}{\alpha} \cos \theta \right), \\ A_2(\xi, \eta) &= \frac{1}{\alpha^2} A_1 \left(\frac{\xi}{\alpha} \cos \theta - \frac{\eta}{\alpha} \sin \theta, \frac{\xi}{\alpha} \sin \theta + \frac{\eta}{\alpha} \cos \theta \right). \end{aligned}$$

Proof. An idea of a proof is taken from [8], [20]. Let us suppose functions

$$\begin{aligned} f_2(x, y) &= f_1(\alpha x \cos \theta - \alpha y \sin \theta - x_0, \alpha x \sin \theta + \alpha y \cos \theta - y_0), \\ f_3(x, y) &= f_1(\alpha x \cos \theta - \alpha y \sin \theta, \alpha x \sin \theta + \alpha y \cos \theta), \\ f_4(x, y) &= f_1(x \cos \theta - y \sin \theta, x \sin \theta + y \cos \theta). \end{aligned}$$

Then by successive application of theorems 2.11, 2.12, 2.13 we obtain relations for Fourier spectra of functions

$$\begin{aligned} F_2(\xi, \eta) &= F_3(\xi, \eta)e^{-i(\xi x_0 + \eta y_0)} = \\ &= \frac{1}{\alpha^2} F_4\left(\frac{\xi}{\alpha}, \frac{\eta}{\alpha}\right) e^{-i(\xi x_0 + \eta y_0)} = \\ &= \frac{1}{\alpha^2} e^{-i(\xi x_0 + \eta y_0)} F_1\left(\frac{\xi}{\alpha} \cos \theta - \frac{\eta}{\alpha} \sin \theta, \frac{\xi}{\alpha} \sin \theta + \frac{\eta}{\alpha} \cos \theta\right). \end{aligned}$$

Analogously for amplitude spectra we obtain

$$\begin{aligned} A_2(\xi, \eta) &= A_3(\xi, \eta) = \\ &= \frac{1}{\alpha^2} A_4\left(\frac{\xi}{\alpha}, \frac{\eta}{\alpha}\right) = \\ &= \frac{1}{\alpha^2} A_1\left(\frac{\xi}{\alpha} \cos \theta - \frac{\eta}{\alpha} \sin \theta, \frac{\xi}{\alpha} \sin \theta + \frac{\eta}{\alpha} \cos \theta\right). \end{aligned}$$

□

2.4.4 Convolution

Definition 2.15 (Convolution) Let functions $f_1, f_2 \in \mathcal{L}(\mathbb{R}^2)$. The *convolution* $f_1 * f_2$ [1] is a function defined by

$$f_1(x, y) * f_2(x, y) = \iint_{\mathbb{R}^2} f_1(s, t) f_2(x - s, y - t) ds dt.$$

Remark 2.7 The function f_2 in the definition 2.15 is called *convolution kernel* or simply *kernel*.

Intuitively convolution can be taken as a response of function f_1 to convolution kernel f_2 shifted by values x and y along axes. Convolution is often used for various image processing methods, typically when calculating pixel values depending on neighbourhood pixels. The kernel is mostly restricted to area according to size of the neighbourhood we wish to consider. Outside the area, we define the kernel function f_2 to be identically zero. The technique is used in the definition of image interpolation methods in section 2.2. Furthermore let us mention some properties of convolution as well as its discrete version which can be used later to compute phase correlation function.

Theorem 2.16 [8] Let functions $f_1, f_2 \in \mathcal{L}(\mathbb{R}^2)$ and let F_1, F_2 be their corresponding Fourier spectra. Then it holds

$$\mathcal{F}\{f_1(x, y) * f_2(x, y)\} = F_1(\xi, \eta) \cdot F_2(\xi, \eta).$$

Remark 2.8 The proof of theorem 2.16 is stated in [1].

Theorem 2.17 [8] Let functions $f_1, f_2 \in \mathcal{L}(\mathbb{R}^2)$ and let F_1, F_2 be their corresponding Fourier spectra. Furthermore let f_1 and f_2 be continuous functions. Then it holds

$$\mathcal{F}\{f_1(x, y) \cdot f_2(x, y)\} = \frac{1}{4\pi^2} F_1(\xi, \eta) * F_2(\xi, \eta).$$

Remark 2.9 The proof of theorem 2.17 is stated in [8].

Definition 2.18 (Discrete convolution) Let functions f_1, f_2 be functions $\{0, 1, \dots, N - 1\}^2 \rightarrow \mathbb{C}, N \in \mathbb{N}$. The *discrete convolution* $f_1 * f_2$ [1] is a function defined by

$$f_1(x, y) * f_2(x, y) = \sum_{s=0}^{N-1} \sum_{t=0}^{N-1} f_1(s, t) f_2(x - s, y - t).$$

Theorem 2.19 [8] Let functions $f_1, f_2 : \{0, 1, \dots, N - 1\}^2 \rightarrow \mathbb{C}, N \in \mathbb{N}$ and let F_1, F_2 be their corresponding Fourier spectra. Then it holds

$$\mathcal{D}\{f_1(x, y) * f_2(x, y)\} = F_1(\xi, \eta) \cdot F_2(\xi, \eta).$$

Remark 2.10 The proof of theorem 2.19 is stated in [8].

Theorem 2.20 [8] Let functions $f_1, f_2 : \{0, 1, \dots, N - 1\}^2 \rightarrow \mathbb{C}, N \in \mathbb{N}$ and let F_1, F_2 be their corresponding Fourier spectra. Then it holds

$$\mathcal{D}\{f_1(x, y) \cdot f_2(x, y)\} = \frac{1}{N^2} F_1(\xi, \eta) * F_2(\xi, \eta).$$

Remark 2.11 The proof of theorem 2.20 is stated in [8].

2.5 Correlation

Phase correlation is a handy tool for image registration. Initially was intended as a tool to detect translation transform between two images, however using techniques such as logarithmic-polar coordinates, we can reformulate the problem of scale and rotation transform to translation transform.

2.5.1 Complex conjugate functions

Firstly let us denote F^* to be a complex conjugate function to Fourier spectrum F . We remind relations between complex conjugate function and its Fourier spectrum. Specific relations hold when f is a real function. This condition satisfies every image, we will work with.

Theorem 2.21 [8] Let function $f \in \mathcal{L}(\mathbb{R}^2)$ and let F be its Fourier spectrum. The Fourier spectrum of function f^* (complex conjugate to f) is a complex conjugate Fourier spectrum F^* to F with reversed axes, i.e. in every point where f be continuous it holds

$$\mathcal{F}\{f^*(x, y)\} = F^*(-\xi, -\eta).$$

Proof. The proof is taken from [14].

$$\begin{aligned} \mathcal{F}\{f^*(x, y)\} &= \int_{-\infty}^{\infty} \int_{-\infty}^{\infty} f^*(x, y) e^{-i(x\xi + y\eta)} dx dy = \int_{-\infty}^{\infty} \int_{-\infty}^{\infty} f^*(x, y) e^{i(-x\xi - y\eta)} dx dy = \\ &= \left(\int_{-\infty}^{\infty} \int_{-\infty}^{\infty} f(x, y) e^{-i[x(-\xi) + y(-\eta)]} dx dy \right)^* = F^*(-\xi, -\eta), \end{aligned}$$

because for $a \in \mathbb{R}$ is

$$\begin{aligned} e^{ia} &= \cos a + i \sin a, \\ e^{-ia} &= \cos a + i \sin(-a) = \cos a - i \sin a. \end{aligned}$$

Hence

$$e^{ia} = (e^{-ia})^*.$$

□

Theorem 2.22 [8] Let $f \in \mathcal{L}(\mathbb{R}^2)$ and let $F \in \mathcal{L}(\mathbb{R}^2)$ be its Fourier spectrum. Let f be continuous. Then the inverse Fourier transform of complex conjugate Fourier spectrum F^* to spectrum F is the complex conjugate function f^* to function f with reversed axes, i.e. in every point where f is continuous it holds

$$\mathcal{F}^{-1}\{F^*(\xi, \eta)\} = f^*(-x, -y).$$

Proof. The proof is taken from [14].

$$\begin{aligned} \mathcal{F}^{-1}\{F^*(\xi, \eta)\} &= \frac{1}{4\pi^2} \int_{-\infty}^{\infty} \int_{-\infty}^{\infty} F^*(\xi, \eta) e^{i(\xi x + \eta y)} d\xi d\eta = \frac{1}{4\pi^2} \int_{-\infty}^{\infty} \int_{-\infty}^{\infty} F^*(\xi, \eta) e^{-i(-\xi x - \eta y)} d\xi d\eta = \\ &= \left(\frac{1}{4\pi^2} \int_{-\infty}^{\infty} \int_{-\infty}^{\infty} F(\xi, \eta) e^{i[\xi(-x) + \eta(-y)]} d\xi d\eta \right)^* = f^*(-x, -y). \end{aligned}$$

□

Theorem 2.23 [8] Let $f \in \mathcal{L}(\mathbb{R}^2)$ and let $F \in \mathcal{L}(\mathbb{R}^2)$ be its Fourier spectrum. Let f be continuous function. f is a real function, i.e.

$$f(x, y) = f^*(x, y), \quad \forall (x, y) \in \mathbb{R}^2,$$

if and only if

$$F(\xi, \eta) = F^*(-\xi, -\eta).$$

Proof. The proof is taken from [14].

(a) Let f be a real function. Then from theorem 2.21 it follows

$$F(\xi, \eta) = \mathcal{F} \{f(x, y)\} = \mathcal{F} \{f^*(x, y)\} = F^*(-\xi, -\eta).$$

(b) Let $F(\xi, \eta) = F^*(-\xi, -\eta)$. Then from theorem 2.22 it follows

$$f(x, y) = \mathcal{F}^{-1} \{F(\xi, \eta)\} = \mathcal{F}^{-1} \{F^*(-\xi, -\eta)\} = f^*(x, y).$$

□

Corollary 2.24 [8] Let $f \in \mathcal{L}(\mathbb{R}^2)$ be a real function and let F be its Fourier spectrum. Then

$$A(\xi, \eta) = A(-\xi, -\eta).$$

Proof. This statement is a consequence of theorem 2.21. □

Corollary 2.25 [8] Let $f \in \mathcal{L}(\mathbb{R}^2)$ be a real continuous function and let $F \in \mathcal{L}(\mathbb{R}^2)$ be its Fourier spectrum. Further let $G : \mathbb{R}^2 \rightarrow \mathbb{R}$ be a bounded real valued function, such that

$$G(\xi, \eta) = G(-\xi, -\eta).$$

Then $\mathcal{F}^{-1} \{F(\xi, \eta) \cdot G(\xi, \eta)\}$ is a real function.

Proof. The proof is taken from [8].

According to theorem 2.23, if f is a real function, then

$$F(\xi, \eta) = F^*(-\xi, -\eta).$$

Multiplying the equality by G , we obtain

$$F(\xi, \eta) \cdot G(\xi, \eta) = F^*(-\xi, -\eta) \cdot G(-\xi, -\eta) = (F(-\xi, -\eta) \cdot G(-\xi, -\eta))^*.$$

Since G is bounded, the existence of an inverse Fourier transform is ensured. Then again according to theorem 2.23

$$F(\xi, \eta) = F^*(-\xi, -\eta)$$

is a real function. □

2.5.2 Phase correlation function

Definition 2.26 (Phase correlation function) Let functions $f_1, f_2 \in \mathcal{L}(\mathbb{R}^2)$ have corresponding Fourier spectra F_1, F_2 . *Phase correlation function* [8] is a function $P_{f_1, f_2} : \mathbb{R}^2 \rightarrow \mathbb{C}$ defined by

$$P_{f_1, f_2}(x, y) = \mathcal{F}^{-1} \left\{ \frac{F_1(\xi, \eta) \cdot F_2^*(\xi, \eta)}{|F_1(\xi, \eta) \cdot F_2(\xi, \eta)|} \right\}.$$

Theorem 2.27 (Phase correlation function of shifted functions) [8] Let functions $f_1 \in \mathcal{L}(\mathbb{R}^2)$ and let F_1 be its Fourier spectrum. Let us consider function f_2 such that

$$f_2(x, y) = f_1(x - x_0, y - y_0),$$

where $x_0, y_0 \in \mathbb{R}$ are given numbers. Let F_2 be the Fourier spectrum of function f_2 . Then the phase correlation function of functions f_1, f_2 is the Dirac δ -distribution function shifted by $(-x_0, -y_0)$, hence

$$P_{f_1, f_2}(x, y) = \delta(x + x_0, y + y_0).$$

Proof. The idea of the proof is taken from [8]. According to theorem 2.11 (Shift theorem) the following equality holds

$$P_{f_1, f_2}(x, y) = \mathcal{F}^{-1} \left\{ \frac{F_1(\xi, \eta) \cdot F_1^*(\xi, \eta)(e^{-i(\xi x_0 + \eta y_0)})^*}{|F_1(\xi, \eta) \cdot F_1(\xi, \eta)(e^{-i(\xi x_0 + \eta y_0)})|} \right\} = \mathcal{F}^{-1} \{ e^{i(\xi x_0 + \eta y_0)} \}.$$

According to [8] is the Dirac δ -distribution function shifted by (x_0, y_0) equal to

$$\delta(x - x_0, y - y_0) = \mathcal{F}^{-1} \{ e^{-i(\xi x_0 + \eta y_0)} \}.$$

Therefore

$$P_{f_1, f_2}(x, y) = \mathcal{F}^{-1} \{ e^{i(\xi x_0 + \eta y_0)} \} = \mathcal{F}^{-1} \{ e^{-i\xi(-x_0) - i\eta(-y_0)} \} = \delta(x + x_0, y + y_0).$$

□

Fourier spectra involved in the definition 2.26 may attain zero value in certain points. In this case the denominator is equal to zero and the fraction itself would not be defined. Therefore in order to ensure, that our fraction will remain in bounds of our assumptions for functions suitable for Fourier and inverse Fourier transform, we will slightly change the denominator and introduce the concept of a semi-phase correlation function.

Definition 2.28 (Semi-phase correlation function) [8] Let functions $f_1, f_2 \in \mathcal{L}(\mathbb{R}^2)$ have their corresponding Fourier spectra F_1, F_2 . Further let $p, q \in \mathbb{R}^+$ be arbitrary positive fixed numbers. *Semi-phase correlation function* is a function $P_{f_1, f_2}^{p, q} : \mathbb{R}^2 \rightarrow \mathbb{C}$ defined by

$$P_{f_1, f_2}^{p, q}(x, y) = \mathcal{F}^{-1} \left\{ \frac{F_1(\xi, \eta) \cdot F_2^*(\xi, \eta)}{(|F_1(\xi, \eta)| + p) \cdot (|F_2(\xi, \eta)| + q)} \right\}.$$

Theorem 2.29 Let $f_1, f_2 \in \mathcal{L}(\mathbb{R}^2)$ be real function with corresponding Fourier spectra F_1, F_2 and amplitude spectra A_1, A_2 . Further let us fix numbers $p, q \in \mathbb{R}^+$. Then the semi-phase correlation function [8]

$$P_{f_1, f_2}^{p, q}(x, y) = \mathcal{F}^{-1} \left\{ \frac{F_1(\xi, \eta) \cdot F_2^*(\xi, \eta)}{(|A_1(\xi, \eta)| + p) \cdot (|A_2(\xi, \eta)| + q)} \right\}.$$

of functions f_1, f_2 with parameters p, q is a real function.

The proof of theorem 2.29 is listed in [8]. It uses corollaries of theorems 2.24, 2.25 and properties of convolution.

According to previous theorems and definitions in the case of two shifted real functions f_1 and f_2 , the phase correlation function should have the form of Dirac δ -distribution function shifted by (x_0, y_0) . In a case of real images with consideration of different illumination and noise influence, the function will contain more local maxima. Nevertheless the phase correlation method is quite robust and therefore we can still stick to searching for a global maximum of a function as the value of other local ones will be nowhere near the value of the global one. The position of maximum (x_0, y_0) corresponds to the shift vector between our considered images.

The uncertainty may occur in cases of images not suitable for phase correlations, such as

- images of periodic structures,
- images where the noise representation outbalances signal information.

2.5.3 Sub-pixel precision phase-correlation

The position (x_0, y_0) of the maximum of phase correlation function (semi-phase correlation function respectively) determines the shift vector between inspected images f_1 and f_2 . This is an integer solution. We would like to get closer to real shift vector with sub-pixel accuracy. The inaccuracy caused by integer rounding can cause large errors, especially when determining scale and rotation changes. One of the simplest ways to get a better estimation of real shift vector is to use geometric moments to calculate weighted centroid of pixels in the neighbourhood of the found maximum.

The idea is that the peak of phase correlation function takes not only single pixel but whole neighbourhood of pixels. The defocus of the peak depends largely on selected parameters of *low-pass high-pass weight function* (see subsection 2.6.2) used for computing phase correlation function (how much we attenuate high frequencies).

Definition 2.30 (Geometric moment) Let (x_0, y_0) be a given point and r the given radius. Then the *geometric moment of order k, l* [16] is given by following formula

$$M_{k,l} = \sum_{x^2+y^2 < r} \sum x^k y^l P_{f_1, f_2}^{p,q}(x_0 + x, y_0 + y), \quad k, l \in \mathbb{N},$$

where, $P_{f_1, f_2}^{p,q}$ is the semi-phase correlation function (see the definition 2.28).

Remark 2.12 The geometric moment $M_{0,0}$ is the overall intensity of the image (respectively of selected neighbourhood).

Definition 2.31 (Weighted centroid) The *weighted centroid* or *center of mass* is defined as

$$(x_1, y_1) = \left(\frac{M_{1,0}}{M_{0,0}}, \frac{M_{0,1}}{M_{0,0}} \right).$$

2.5.4 Polar coordinates

From phase correlation function we are able to determine translation transform between two images. With slight reformulation, we can use the same concept also for detecting image scale and rotation changes. For example using well-known transformation to polar coordinates, the initial image rotation transform will become a problem of translation on angle axis φ .

Definition 2.32 (Transformation to polar coordinates) Let $f : \mathbb{R}^2 \rightarrow \mathbb{C}$. Let us denote $f^p : \langle 0, \infty \rangle \times \langle 0, 2\pi \rangle \rightarrow \mathbb{C}(\varrho, \varphi)$ the *transformation to polar coordinates* ϱ, φ of function f [8] such that ϱ satisfies

$$\varrho = \sqrt{x^2 + y^2}$$

and φ is the solution to

$$x = \varrho \cos \varphi,$$

$$y = \varrho \sin \varphi.$$

2.5.5 Logarithmic-polar coordinates

Similarly, we can introduce a suitable transform, which displays not only rotation but also scale change as translation on single axis.

Definition 2.33 (Transformation to logarithmic-polar coordinates) Let $f : \mathbb{R}^2 \rightarrow \mathbb{C}$. The function $f^{lp} : \mathbb{R} \times \langle 0, 2\pi \rangle \rightarrow \mathbb{C}(\varrho, \varphi)$ is called the *transformation to logarithmic-polar coordinates* of function f [8] if ϱ satisfies

$$e^\varrho = \sqrt{x^2 + y^2},$$

and φ is the solution to

$$x = e^\varrho \cos \varphi,$$

$$y = e^\varrho \sin \varphi.$$

If the mutual transformation between couple of images includes all translation, rotation and scale changes, we have to separate the problem of translation transform from others, otherwise the transformation to logarithmic-polar coordinates will not be applicable.

Therefore instead of using original images, we will transform to logarithmic-polar coordinates their amplitude spectra. We know that translation transform does not change the amplitude spectrum thanks to the theorem 2.11 (Shift theorem). Hence, firstly we investigate rotation and scale changes using amplitude spectra and than we can return to the remaining translation transform.

However we have to be aware also of the corollary 2.24 which states

$$A(\xi, \eta) = A(-\xi, -\eta),$$

causing the angle axis to be only π and not 2π periodic. We have to be aware of this restriction while evaluating the angle of rotation change from phase correlation function. If we get the angle θ from phase correlation function, we know the actual transform will be either θ or $\theta + \pi$. We can consider both changes, redo the rotation and compare both images with the reference image by using phase correlation function again. The proper angle is than determined by greater from both phase correlation functions maximum values.

2.6 Weight functions

2.6.1 Window function

Let us remind the idea of Fourier transform. Basically it decomposes the signal (our image) into a set of periodic trigonometric functions. Let our image of dimensions $[M, N]$ be described by function f . In that case, f is discrete function, which is identically equal to zero except the rectangular region $\langle 0, M - 1 \rangle \times \langle 0, N - 1 \rangle$. But the (2D) Fourier transform is much more suitable (and simpler) when describing periodic functions on \mathbb{R}^2 [11]. Therefore it is convenient to extend f to a periodic function \tilde{f} as follows

$$\tilde{f}(x, y) = f(x \bmod M, y \bmod N), \quad \text{where } x, y \in \mathbb{Z}.$$

Fourier transform is very sensitive to rapid changes of function values. In general \tilde{f} will have lines of discontinuities pM and qN , where $p, q \in \mathbb{Z}$ which could have a dramatic impact on the Fourier transform representation and possible change the location of phase correlation function's maximum leading us to wrong image registration results. Hence a little modification of f is in place before the extension to \tilde{f} , namely multiplication by so-called window function. The window function preserves values of f around the image center and smoothly diminishes the edge-surrounding pixel values.

Clearly application of window function may also lead to the exclusion of important significant structures around image edges that would help to highlight the maximum of phase correlation function. It is therefore a matter of optimization and finding the balance between small discontinuities and the least amount of lost image information. That may differ a lot according to the type of images we are dealing with.

With respect to our large, rather monotonous images containing no significant structures, it should not matter a lot on the type of window function chosen. Let us introduce only two of such functions.

Definition 2.34 (Window functions) Let sets

$$A = \langle -a, a \rangle \times \langle -b, b \rangle, \quad a, b \in \mathbb{R}_0^+,$$

$$B = \{(x, y); x^2 + y^2 \leq r^2\}, \quad r \in \mathbb{R}_0^+.$$

Let $\sigma \in \mathbb{R}^+$ be a given number. Let $\varrho(X, A)$ be the distance of point $X = (x, y)$ from the set A defined by

$$\varrho(X, A) = \inf\{d \in \mathbb{R}^+, d = \varrho(X, Y), Y \in A\},$$

where $\varrho(X, Y)$ is the Euclidean metric. Then

1. The function

$$g_{GR}(x, y) = e^{(-\frac{\varrho^2(X, A)}{\sigma^2})}$$

is called the *rectangular Gaussian window function* [8].

2. The function

$$g_{GC}(x, y) = e^{-\frac{\varrho^2(X, B)}{\sigma^2}}$$

is called the *circular Gaussian window function* [8].

3. The function

$$g_{HR}(x, y) = \begin{cases} \frac{1}{2} + \frac{1}{2} \cos \frac{\pi \varrho(X, A)}{\sigma} & \text{if } \varrho(X, A) \leq \sigma, \\ 0 & \text{if } \varrho(X, A) > \sigma, \end{cases}$$

is called the *rectangular Hanning window function* [8].

4. The function

$$g_{HC}(x, y) = \begin{cases} \frac{1}{2} + \frac{1}{2} \cos \frac{\pi \varrho(X, B)}{\sigma} & \text{if } \varrho(X, B) \leq \sigma, \\ 0 & \text{if } \varrho(X, B) > \sigma, \end{cases}$$

is called the *circular Hanning window function* [8].

Rectangular window function retains more image information and it computationally faster than the circular one, but does not diminish totally on the edges. Similarly, Gaussian window function will never be zero on edges, but can be negligible by choosing a proper value of σ .

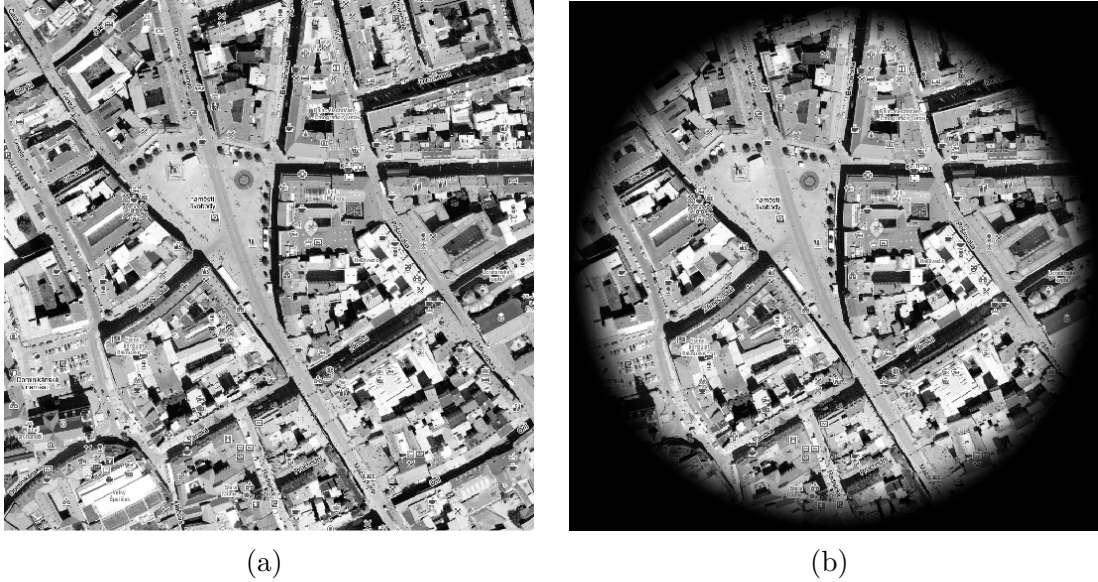


Figure 2.5: Application of circular Hanning window function ([20]).
 (a) Original image.
 (b) Image multiplied by circular Hanning window function.

2.6.2 Low-pass high-pass weight function

In the case of registering real images, noise influence has to be considered. Both additive and impulsive noise are involved. From a Fourier spectrum point of view the noise is present on each spatial frequency but generally its significance increases as the frequency rises. This makes higher frequencies less reliable for proper image registration. We would like to suppress its influence (amplitude) by an appropriate weighted function but again we have to search for a balance. By repressing them we are also reducing the potential accuracy of image registration as the highest frequencies contain information about the smallest structures.

Moreover the lowest spatial frequencies are problematic too. The zero frequency represents the average pixel value and other low frequencies contain information about large

image structures such as diffuse light in the optical system and vignetting. Furthermore they are sensitive to different contrast and brightness of an image.

Due to the facts mentioned above, the overall shape of the required weighted function of spatial frequencies is quite limited and we can define it as follows in the definition below.

Definition 2.35 (Low-pass high-pass weight function) Let $r_1, r_2, \sigma_1, \sigma_2 \in \mathbb{R}^+$ such that $r_1 < r_2$. The function $H_{r_1, \sigma_1}(\xi, \eta) : \mathbb{R}^2 \rightarrow \langle 0, 1 \rangle$ defined as

$$H_{r_1, \sigma_1}(\xi, \eta) = \begin{cases} 0 & \text{if } \frac{4}{N^2}(\xi^2 + \eta^2) < (r_1 - \sigma_1)^2, \\ \frac{1}{2} + \frac{1}{2} \cos \frac{\pi(r_1 - \frac{2}{N} \sqrt{\xi^2 + \eta^2})}{\sigma_1} & \text{if } (r_1 - \sigma_1)^2 \leq \frac{4}{N^2}(\xi^2 + \eta^2) < r_1^2, \\ 1 & \text{else,} \end{cases}$$

is called the *high-pass weight function* [8]. The function $H^{r_2, \sigma_2}(\xi, \eta) : \mathbb{R}^2 \rightarrow \langle 0, 1 \rangle$ defined as

$$H^{r_2, \sigma_2}(\xi, \eta) = \begin{cases} 1 & \text{if } \frac{4}{N^2}(\xi^2 + \eta^2) < r_2^2, \\ \frac{1}{2} + \frac{1}{2} \cos \frac{\pi(r_2 - \frac{2}{N} \sqrt{\xi^2 + \eta^2})}{\sigma_2} & \text{if } r_2^2 \leq \frac{4}{N^2}(\xi^2 + \eta^2) < (r_2 + \sigma_2)^2, \\ 0 & \text{else,} \end{cases}$$

is called the *low-pass weight function* [8]. The function $H_{r_1, \sigma_1}^{r_2, \sigma_2}(\xi, \eta) : \mathbb{R}^2 \rightarrow \langle 0, 1 \rangle$ defined as

$$H_{r_1, \sigma_1}^{r_2, \sigma_2}(\xi, \eta) = H_{r_1, \sigma_1}(\xi, \eta) \cdot H^{r_2, \sigma_2}(\xi, \eta)$$

is called the *low-pass high-pass weight function* [8].

3 Implementation

Now after summarization of required context and mathematical theory we are ready to design and implement an algorithm able to process a couple of images from distinct wavelengths and combine them into a single image in order to receive information about C IV spatial distribution. For the purpose of visualization of distribution in time, a time sequence of images is created resulting in a video.

3.1 Algorithm

The proposed algorithm consists of the following steps:

- Downloading a sequence of images in selected time interval on both 1 600 Å and 1 700 Å wavelengths.
- Removing calibration images.
- Sorting 1 600 Å images by time.
- Finding the closest 1 700 Å image for each 1 600 Å image.
- Registering of each corresponding image couple.
- Computing multiplicative function.
- Merging images into a single color image.
- Applying histogram modification.
- Creating a video of merged images.

In the following subsections, we will describe each step in further details.

3.1.1 FITS files download

As was already mentioned in subsection 1.2.1, we can filter our required images on VSO web page [22]. It will give us a list of urls corresponding to each FITS file. This list is exportable to .csv file. We can easily rename the file to text file .txt and use *curl* to download all FITS files through url list in a text file. In our case the *curl for Windows 7.66.0* was used [4].

3.1.2 Image preprocessing

FITS files downloaded from VSO have been already preprocessed. According to [24], following operations were applied:

- overscan pixel removal,
- dark pedestal, dark current and flat field corrections,
- bad pixel and cosmic-ray spikes removal,

- image rescaled to integer,
- image flipped to match Solar North pole.

We have to keep in mind, that some of those calibration images may be present in our downloaded FITS files and eliminate them. For example, *dark frames*, used for correcting zero pixel intensity level can be detected by computing arithmetic mean of image pixel values which will be much smaller in comparison with a regular image (usually lower than 1) or simply checking the header keyword `IMG_TYPE`.

If it is a regular image then the keyword has value `LIGHT` otherwise `DARK` in the case of *dark frame* image.

3.1.3 Image registration

Image registration can be done by phase correlation method mentioned in section 2.5 to find scale, rotation and translation parameters of mutual image transformation. Thanks to the FITS header information of SDO images, we can achieve the image couple registration much faster. Each FITS image has in header a keyword `R_SUN` followed by float number representing Sun's radius in pixels. Therefore the ratio of those values of the first and second image gives us the scale change parameter. Similarly the keyword `CROTA2` represents an angle to reference image axes. The difference between both images values gives us mutual rotation transformation angle. And lastly, the translation parameters can be obtained from keywords `CRPIX1` and `CRPIX2` being the Sun disk center location in pixel (assuming pixel numbering starts from 1).

After obtaining all three parameters we have to choose an appropriate interpolation method used when applying the transformation. The nearest neighbour is the fastest one, but at the same time very inaccurate. The bilinear interpolation blurs the edges and decreases the dynamic range of an image (more details and demonstrative images are stated in [21]). But it preserves the total intensity of an image, which is important for us as we want to fit two images together. Biquadratic and bicubic interpolation better preserve the sharpness of edges but changes more the original information, which leads to worse results in later merging step of two images. Strange artifacts arise in the resulting composed image (see section 3.3). Besides, the required computational time is greatly increased.

3.1.4 Multiplicative function computation

Ignoring the discrete set of emitting and absorbing frequencies, the Sun can be seen as a black body with surface temperature 5800 Kelvins as it is depicted in the figure 3.1. Each couple of images represents a signal from the Sun in a narrow band pass. Both wavelengths 1600 Å and 1700 Å contributes very little proportionally to radiation intensity of the Sun on other wavelengths. Also, despite being relatively close to each other, the radiation on the shorter wavelength is significantly weaker. The exposure time of 1600 Å images is fixed at 2.9 seconds, while 1700 Å images at 1 second. Still, the intensity of 1700 Å images is roughly five times higher.

Therefore before combining images from both wavelengths together, a multiplication of one of the image pixels' values by an appropriate constant is required. Moreover this constant may vary with respect to the radius from the Sun disk center in a picture. With increasing radius, we are looking at the Sun at different angles. This causes the radiation from lower

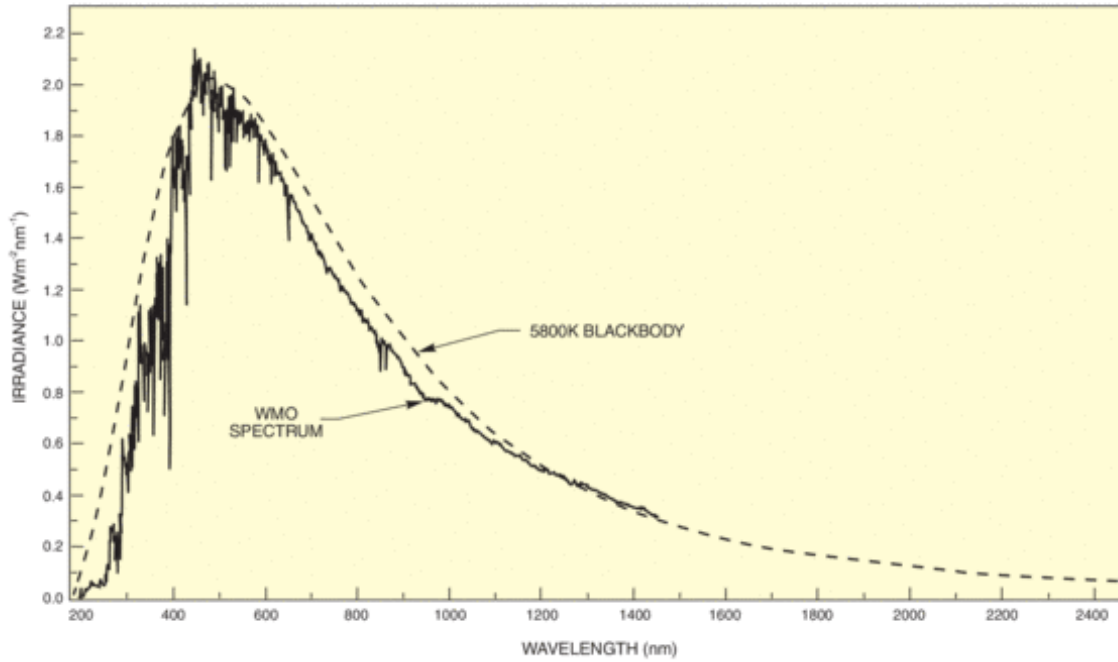


Figure 3.1: Spectrum of the radiation outside the Earth’s atmosphere compared to the spectrum of a 5800 K blackbody ([23]).

Sun’s atmosphere layers to travel through thicker and thicker upper layers. The permeability of those layers differs for 1600 Å and 1700 Å wavelengths. Hence instead of constant, we shall look for a multiplicative function depending on that radius.

To achieve the lowest calculation errors possible, we designed the multiplicative function in such a way, that pixel values of 1600 Å image multiplied by our multiplicative function fits 1700 Å image pixel values. Since 1600 Å images have lower absolute pixel intensities, the multiplicative function will attain values greater or equal to one and relative rounding error of multiplied pixel values to integer will be smaller in comparison with the case when we would compute the inverse function and apply it on 1700 Å image pixel values.

Registered images are divided into annuli with a constant difference of outer and inner radius. On each of the annulus pixels, a sort of Kappa Sigma clipping method is applied to remove statistically very distinct pixel values. Rather than computing mean, we use it to get better representative median. Next, the ratio of medians from both images is computed for corresponding annuli, giving us the multiplicative function. Lastly, the 1600 Å image is multiplied by computed multiplicative function, while the exact multiple is obtained by linear interpolation between two closest annuli ratios with respect to the distance from the Sun disk center.

Further study of suitable multiplicative function is discussed in section 3.2.

3.1.5 Image merging

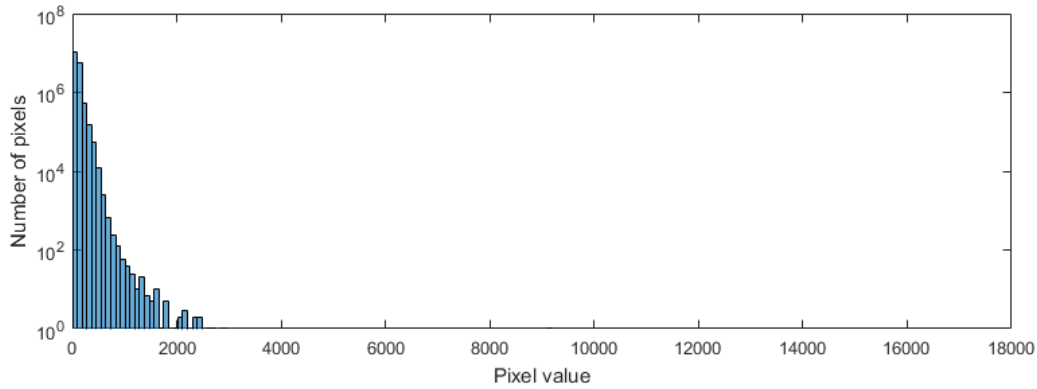
The basic idea is to take two images with corresponding intensities (corrected by multiplicative function) and assign its pixel values to different color channels. As we are working with red-green-blue color system (RGB), we assign one image to one channel and the second one to the remaining two channels. The result should be a gray-scale image with highlighted

colorful areas containing carbon C IV while the color is affected by selected channel combination. We assigned the 1 700 Å image to the green channel and 1 600 Å image (which includes records of carbon C IV) to the red and blue channel. Therefore all the areas containing carbon C IV will be highlighted with magenta color.

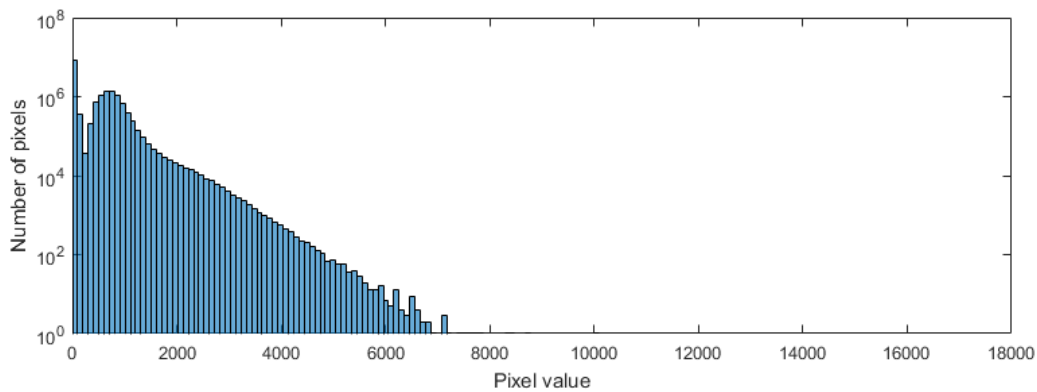
3.1.6 Histogram modification

Our images of the Sun have very large dynamic range, namely 15 bits per pixel are used. Pixels can therefore attain values from -16383 to 16383 .

Histograms of both wavelengths images have a monomodal character for most of the time. As an example, in the figure 3.2, there are histograms of images just before a great eruption occurred on October 24, 2014. The peak is located very close to the zero value intensity and represents the Sun disk pixels. If a larger eruption occurs in the image, the histogram becomes bimodal as can be seen in the figure 3.3. The second peak is caused by pixels visualizing the eruption and is located very close to the maximum value of the dynamic range (the blooming effect is present). Therefore most of the image is relatively very dark with just small bright part capturing the eruption. Histograms depicted in the figures 3.2 and 3.3 consist of 100 bins and negative pixel values are counted as zeros.



(a)

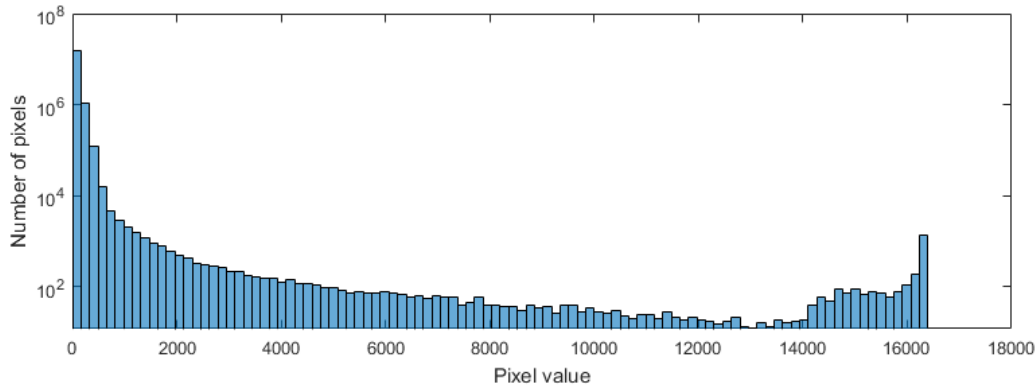


(b)

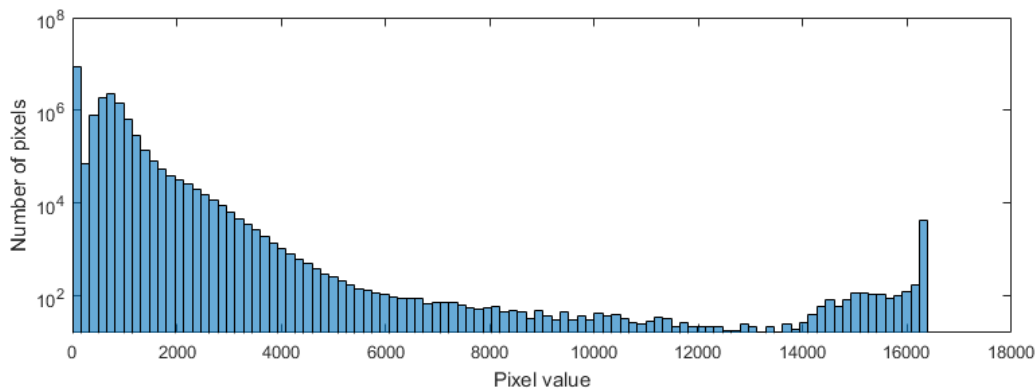
Figure 3.2: Histogram of images before an eruption on October 24, 2014.

(a) Histogram of 1 600 Å image.

(b) Histogram of 1 700 Å image.



(a)



(b)

Figure 3.3: Histogram of images of an ongoing eruption on October 24, 2014.

(a) Histogram of 1600 Å image.

(b) Histogram of 1700 Å image.

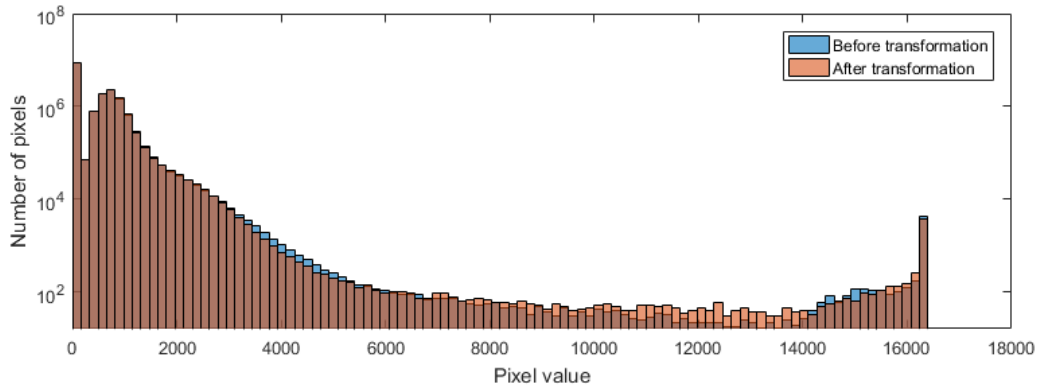
A suitable histogram transformation can be applied to make the image better from a human vision point of view. Standardly used method is gamma transformation (introduced in subsection 2.3.2) with parameter $\gamma = 2.2$. This brings some more light in the image.

In the figure 3.4, there is visible a change in the histogram of 1700 Å image according to used interpolation type for image transformation. The bilinear interpolation does not change the shape of histogram much, whereas biquadratic decreases the pixel value and bicubic does so even more. This could potentially help to visualize images, but on the other hand we are changing the original information quite too much and some unwanted artifacts can arise as described in section 3.3. According to the chosen interpolation method, the multiplicative function may vary a bit. As the histogram remains almost the same when using bilinear interpolation, the change of a multiplicative function with respect to the original images will be negligible.

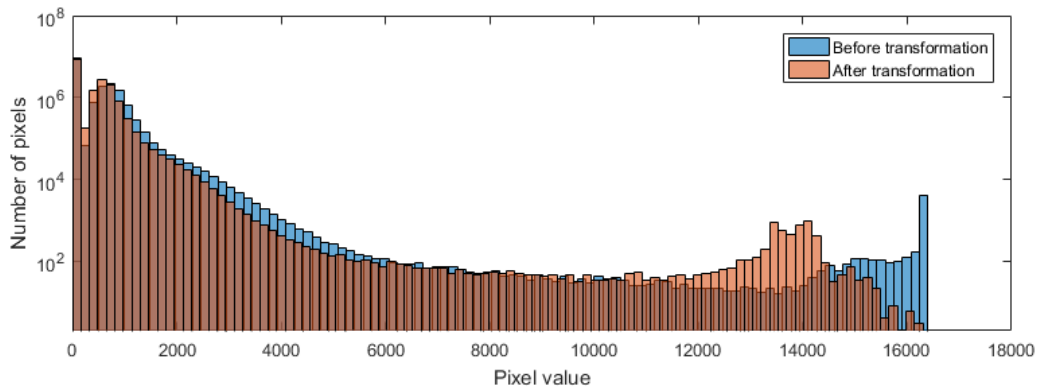
3.1.7 Used libraries

The algorithm was implemented in C# programming language using Microsoft Visual Studio. Following 3rd party packages were used:

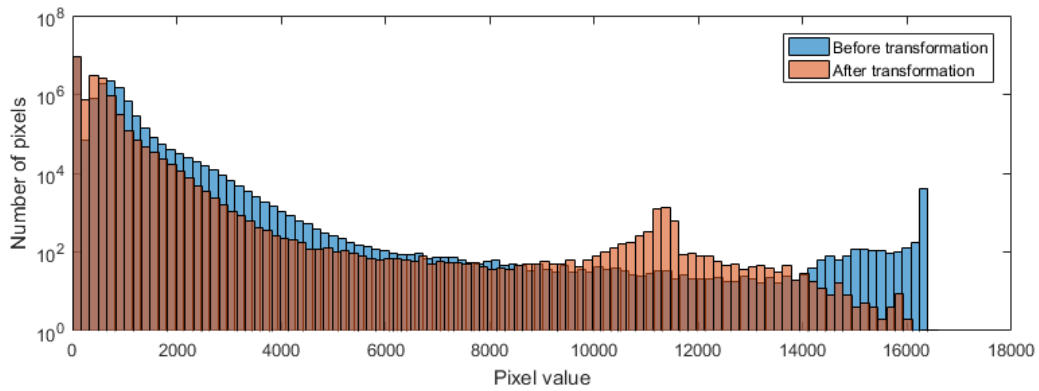
- CSharpFITS,



(a)



(b)



(c)

Figure 3.4: Comparison of histogram of 1700 Å image before and after transformation.

(a) Bilinear interpolation.

(b) Biquadratic interpolation with parameter $a = 1$.

(c) Bicubic interpolation with kernel of size 6.

- SharpAvi.

The package `CSharpFITS` [3] enables simple access to FITS files headers and data units. The package `SharpAvi` [2] helps to create videos of resulting image sequences.

Charts were generated using `Matlab`.

3.2 Multiplicative function results

In the beginning, the figure 3.5 shows inapplicability of constant function multiplication, where the constant is given by the ratio of image medians of pixel values. The resulting image has green shades in disk center and gets magenta on disk edges.

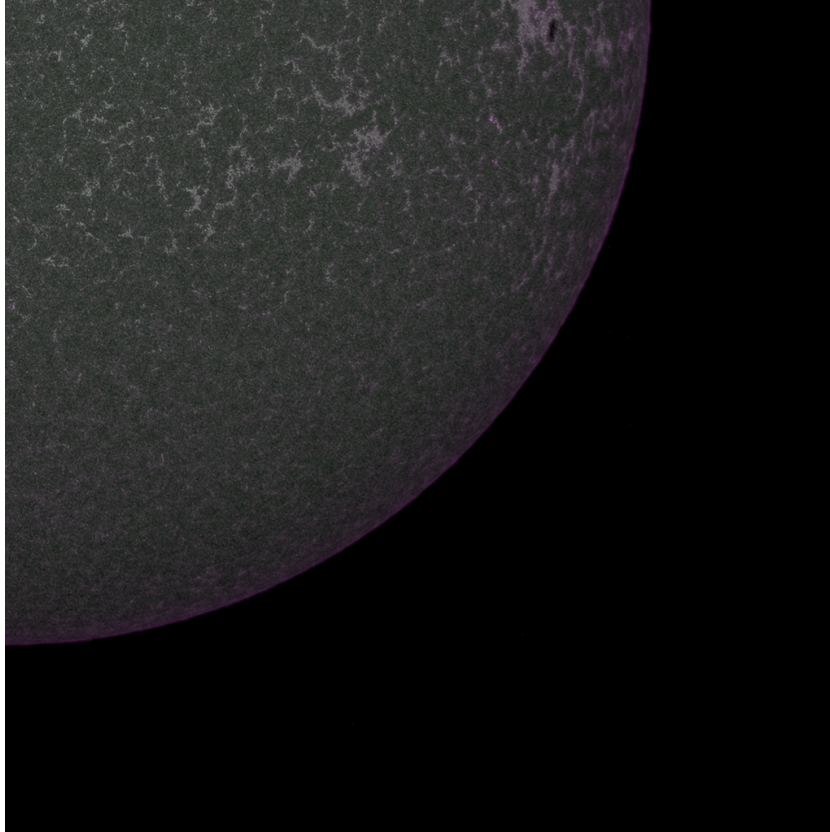


Figure 3.5: Merged images corrected by a constant multiplicative function.

For computing the multiplicative function, annuli of different thickness were tested. From all tested annuli widths, the width of only one pixel was chosen. Looking at the figure 3.6, the reason is obvious. Approaching the edge of the Sun disk around the diameter of 1650 pixels, the multiplicative function changes rapidly and the linear interpolation is no longer effective in computing corresponding function values between two neighbouring steps when using large steps. We need to soften the division. From the figure 3.7 can be seen, that width of one pixel gives satisfying results in final color channel balance and preserves the neutral gray shade.

Furthermore, annuli close to the center contain much less pixels than further ones and requires inadequately large number of images to compute the representative median value of annuli pixel values with decent reliability. But the variation of the angle at which we are looking at the Sun surface is changing relatively slowly and hence the multiplicative function does not have large derivative. That is why it was decided to compute median value for a center circle of radius 100 pixels and after that continue with already mentioned annuli of single pixel width division for further distances.

As we continue to the edges of the image, the median value decreases and zero values may occur. To avoid division by zero, we have to set up a threshold. When one of the medians in the ratio is lower than our selected threshold, the multiplicative function value is set

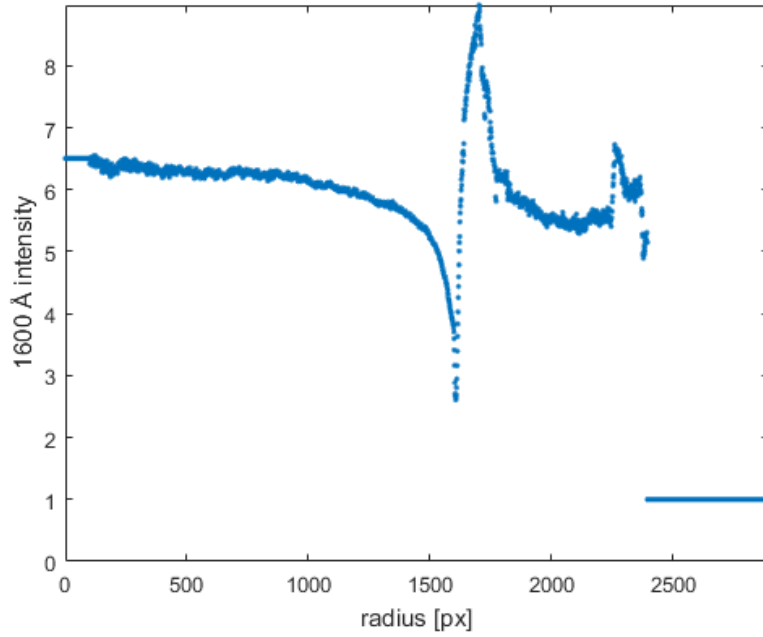
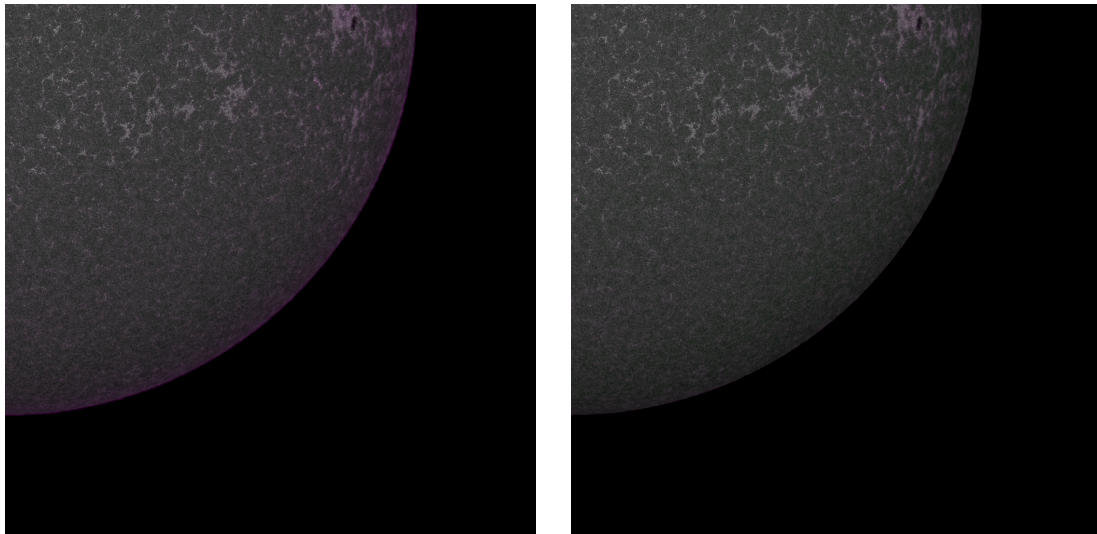


Figure 3.6: Example of a multiplicative function with step size 1 pixel and with center circle radius of 100 pixels.



(a)

(b)

Figure 3.7: Multiplicative function.

(a) Multiplicative function with step of size 16 px.

(b) Multiplicative function with step of size 1 px.

to 1. The threshold in our computation was set to 1. That might lead to some inaccurate estimates of multiplicative function value for annuli with medians close to 1, but regarding the very low pixel values intensity in those annuli, the eventual color channels imbalance will hardly be visible and very small in absolute pixel value difference.

3.2.1 Evolution in time

The computation of the multiplicative function is quite computationally demanding task. Overall processing of images takes a lot of computational time, regarding our intention to create a video consisting of hundreds of processed image couples. As already mentioned in subsection 3.1.4, images on both wavelengths have indeed different exposure times, but they are constant in time. Focusing on performance improvement, one might come to an idea, that we can save some time by precalculating a uniform multiplicative function applicable for all image couples. More luckily this function would be independent of time and therefore applicable also on records from totally different day or even year.

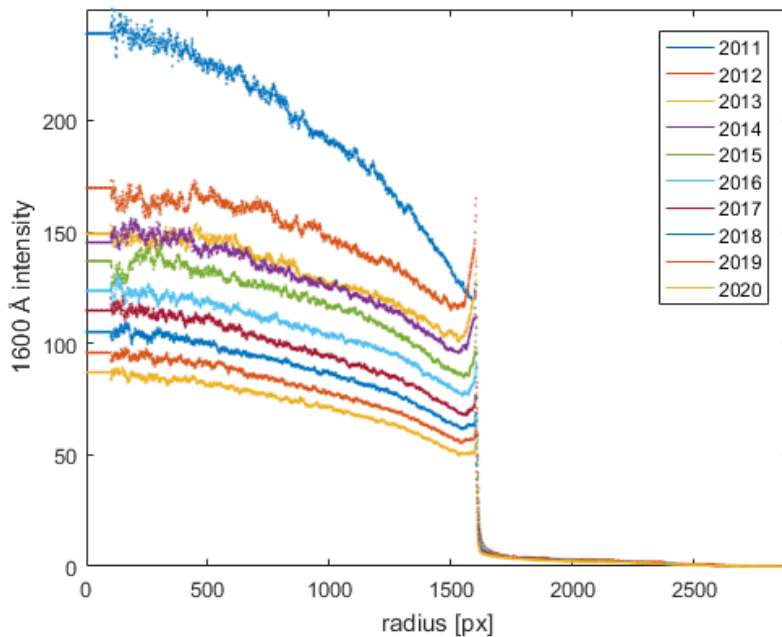


Figure 3.8: Evolution of pixel values on 1600 Å in time.

A brief investigation of multiplicative function's form was held. For each year from 2011 to 2020, ten subsequent images on each wavelength were selected from February 2nd. Then, using Kappa Sigma Clipping method, medians for each annulus were computed. The median function of the radius was calculated for each year. The results for 1600 Å images are summarized in the figure 3.8 and for 1700 Å images in the figure 3.9.

We can see a consistent decrease of pixel value intensities in 1600 Å. Since 2011 intensities dropped almost on one third of its initial values in 2011. Looking at medians of 1700 Å images, the decrease is also visible. But the evolution is not so straightforward as in the first case and the overall relative drop since 2011 is only roughly 30 %.

The final multiplicative functions are in the figure 3.10. Since yearly relative drops of 1600 Å values are bigger than in 1700 Å values, the multiplicative function is increasing in time.

The change of measured total light intensity in time is probably caused by decreasing quantum efficiency (sensitivity) of AIA's CCD chips. Moreover, pixels in the center of a chip are exposed to the strongest radiation and therefore degrading faster. But it does not have to be effect only of chip's sensitivity. The optics and filters might also change its characteristics over time. But it requires an additional study which is not in the scope of this thesis.

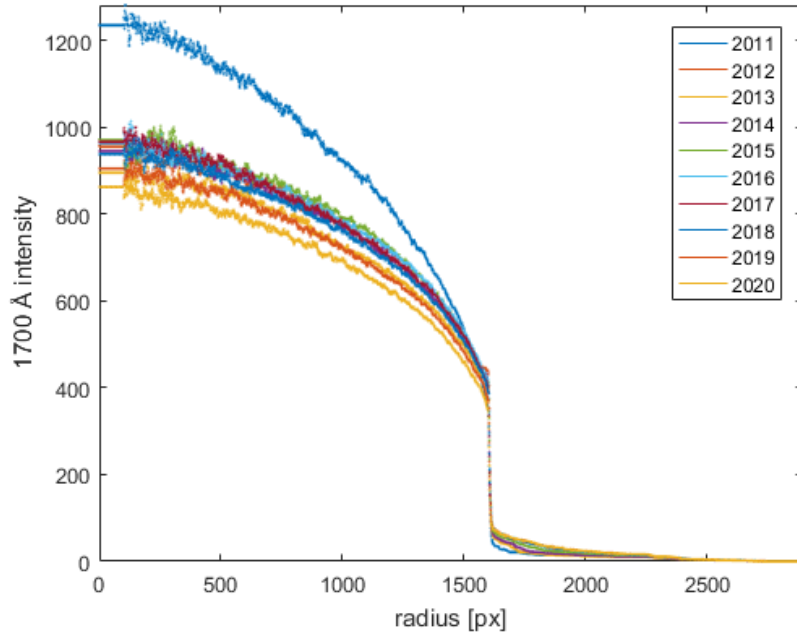


Figure 3.9: Evolution of pixel values on 1700 Å in time.

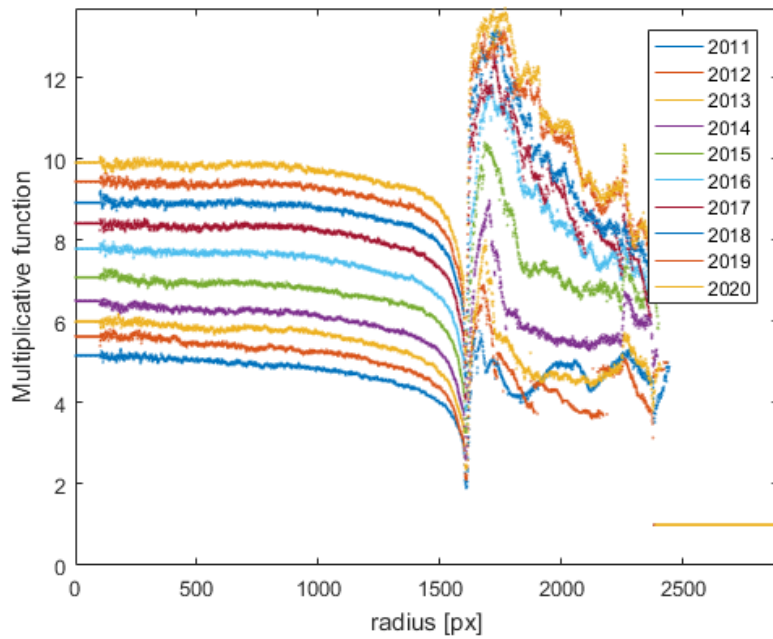


Figure 3.10: Evolution of multiplicative function in time.

As a result of our findings, we are unable to use a unique precalculated multiplicative function, that would be usable for records from any time. We have to calculate it for each set of images individually.

3.3 Resulting images and video

For a demonstration of resulting images, quite a strong eruption on October 24th 2014 was chosen.

Looking at the figure 3.11, you can see a detail of an ongoing eruption. First two pictures a) and b) represents 1600 Å and 1700 Å wavelength respectively with applied gamma correction. Original images were combined into an image c) by

- computing and applying multiplicative function with resolution step 1 px,
- applying gamma correction with $\gamma = 2.2$ while changing zero pixel value to 200 and keeping maximum value the top of original dynamic range (i.e. 2^{14}),
- the modified 1600 Å was assigned to the red and blue color channels of resulting image and the modified 1700 Å was assigned to the green channel.

Finally the picture d) depicts the difference of both images.

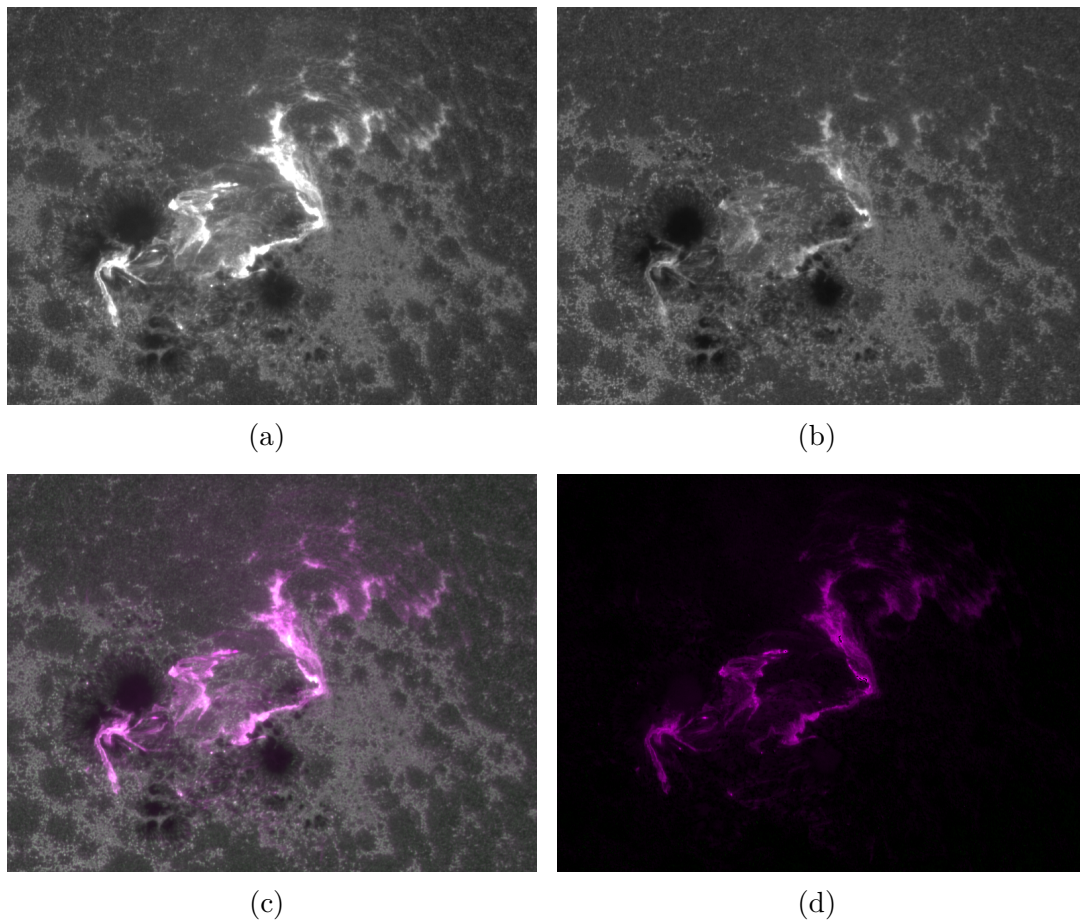


Figure 3.11: The Sun eruption in detail.

- (a) Image on 1600 Å.
- (b) Image on 1700 Å.
- (c) Resulting color image.
- (d) The difference image.

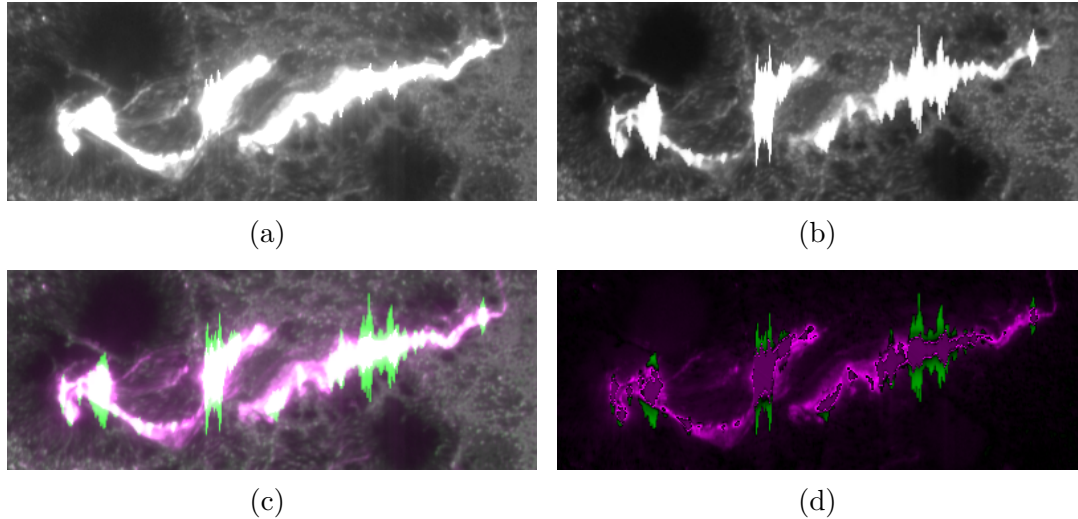


Figure 3.12: The Sun eruption in detail with strong blooming effect.

- (a) Image on 1 600 Å.
- (b) Image on 1 700 Å.
- (c) Resulting color image.
- (d) The difference image.

There is another example from the same eruption in the figure 3.12. Here, the strong blooming effect is present. The intensive light is probably caused by only thin stream along a magnetic field induction line but as it exceeds the maximum pixel capacity of a chip, captured electrons start overflowing to neighbouring pixels, preferring the columnar direction. The effect is stronger in 1 700 Å image because the average intensity on that wavelength is higher than on 1 600 Å wavelength. Some of the pixels will be on top of dynamic range in both images. Hence in those places the information about carbon C IV presence is lost and the corresponding pixel in composed color image will have neutral, white color.

As already discussed in subsection 3.1.6, histograms of images with strong ongoing eruptions have bimodal character with one peak very close to zero pixel values (corresponding to most of background and Sun disk pixel values) and the second one is very close to the top of dynamic range corresponding to flares along magnetic induction lines in the place of an eruption.

The second peak is chopped off at maximum pixel value, so some information is lost and the image is affected by strong blooming effect. Most of the middle range pixel values are unused and the resulting image captures very dark Sun disk and very bright eruption places. To stretch out the low peak of histogram, we can saturate the image. This will make most of Sun disk more locally contrasting.

On the other hand the very bright places will be saturated and lost some contrast and the image noise is also multiplied. The comparison can be seen in the figure 3.13. For the saturated image, the maximum pixel value was set to 6000 after applying the multiplicative function.

In sections 2.2 and subsections 3.1.6 respectively, we discussed expected influence of using different interpolation methods in image transformation. We can now compare it on actual examples of resulting images processed using bilinear, biquadratic and bicubic interpolation respectively in the figure 3.14. You can notice the decrease of intensities while using biquadratic and bicubic interpolation method (corresponding with histogram changes

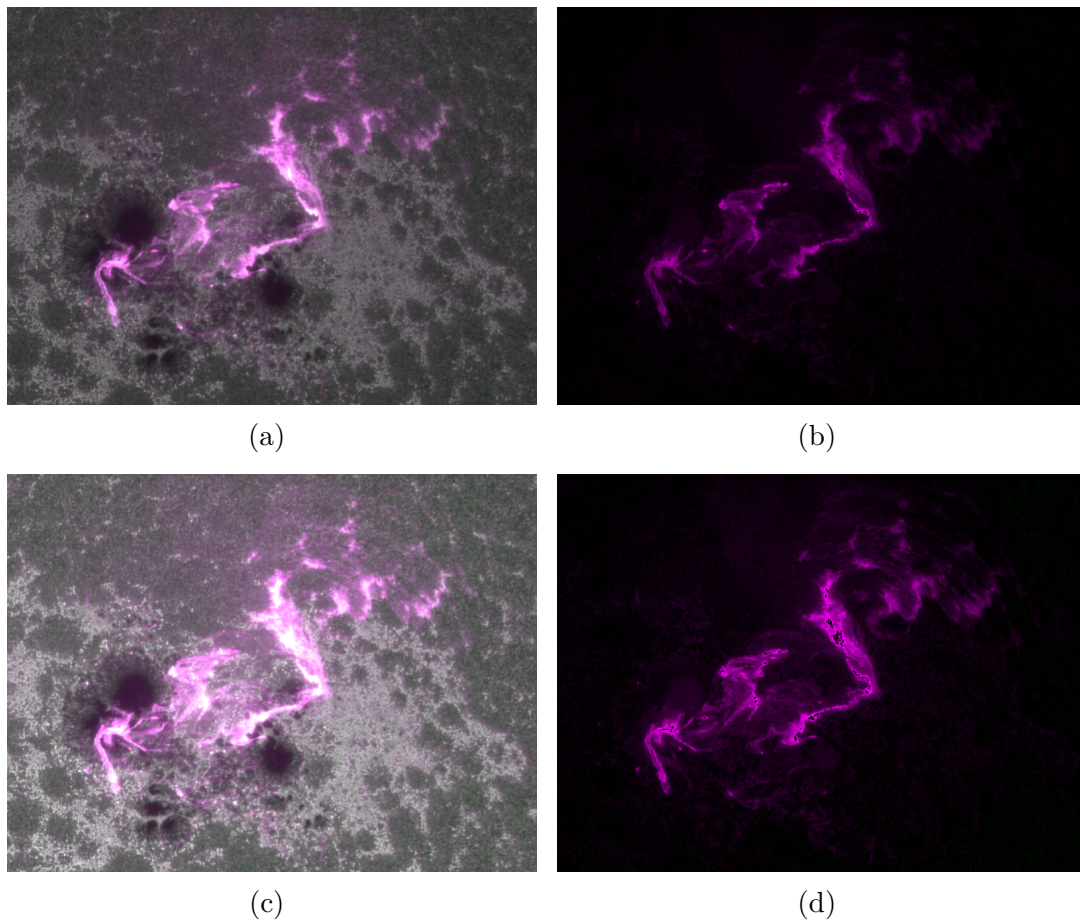


Figure 3.13: Comparison of non saturated and saturated image with saturated pixels with original value over 6000.

- (a) Color non saturated image.
- (b) The difference image of non saturated image.
- (c) Color saturated image.
- (d) The difference image of saturated image.

depicted in subsection 3.1.6). Because the change is not very significant, no gamma correction was applied to make the change more visible.

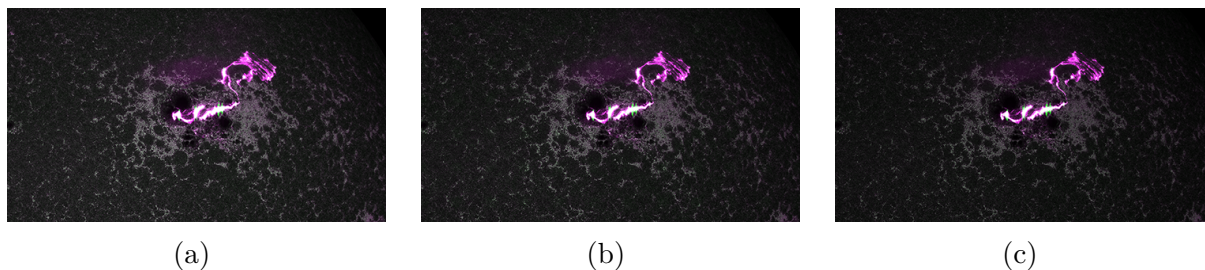
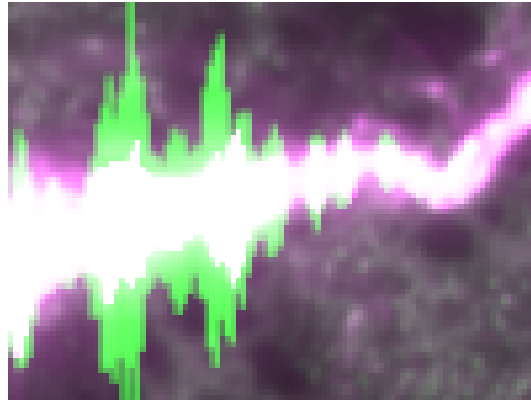
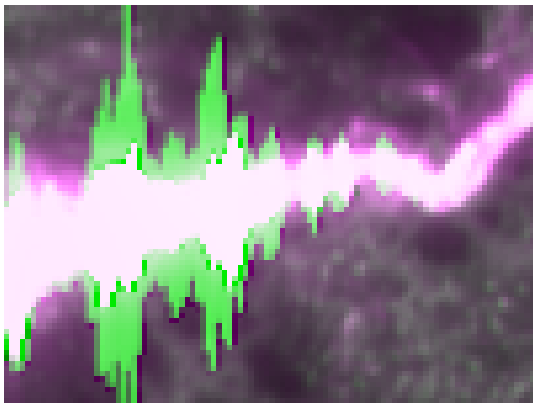


Figure 3.14: Comparison of resulting images with different type of interpolation method used for transformation.

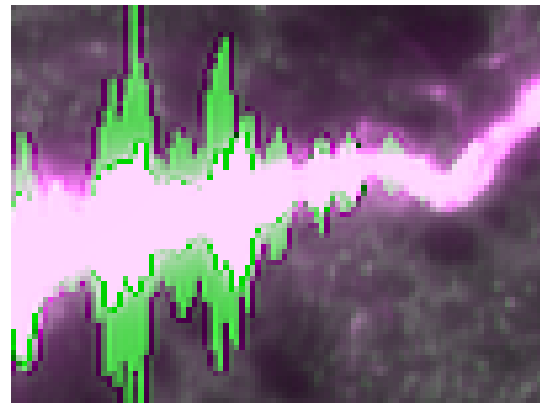
- (a) Bilinear interpolation.
- (b) Biquadratic interpolation with parameter $a = 1$.
- (c) Bicubic interpolation with kernel of size 6.



(a)



(b)



(c)

Figure 3.15: Comparison of edge sharpness in resulting images according to the interpolation method used for transformation.

(a) Bilinear interpolation.

(b) Biquadratic interpolation with parameter $a = 1$.

(c) Bicubic interpolation with kernel of size 6.

In the figure 3.15 you can see in detail the difference of edge sharpness with respect to used interpolation method. The borderline between very bright eruption lines with carbon C IV (and surrounding overflowed pixels) and rest of the Sun disk is blurred in the case of using bilinear interpolation and is significantly sharper for both biquadratic and bicubic interpolation method. This effect is not desirable for our purposes. That is why the bilinear interpolation comes out as the most suitable interpolation.

3.4 Graphical user interface

To create an opportunity to reproduce created images and videos of carbon C IV emissions or study other events in Sun's atmosphere, a graphical user interface (GUI) *Carbon C IV Analyser* was created for *Windows* operating systems. The appearance of GUI is depicted in figures 3.16 and 3.17. Let us describe its components.

On top of GUI you can see section (or panel) called *Directory setup* {1}, where you can set up *Data directory*, which tells the algorithm where to find and save all data. FITS

images are saved into subfolder *fits* and merged images into subfolder *pic*. If they do not exist, subfolders are created automatically once the process is triggered. *FITS files URL links* as the name suggests, is a reference to file that contains links on files from VSO.

Tab menu {2} enables you to switch between tabs *Data selection* and *Histogram modifications and preview*. We will describe both tabs in the following two subsections.

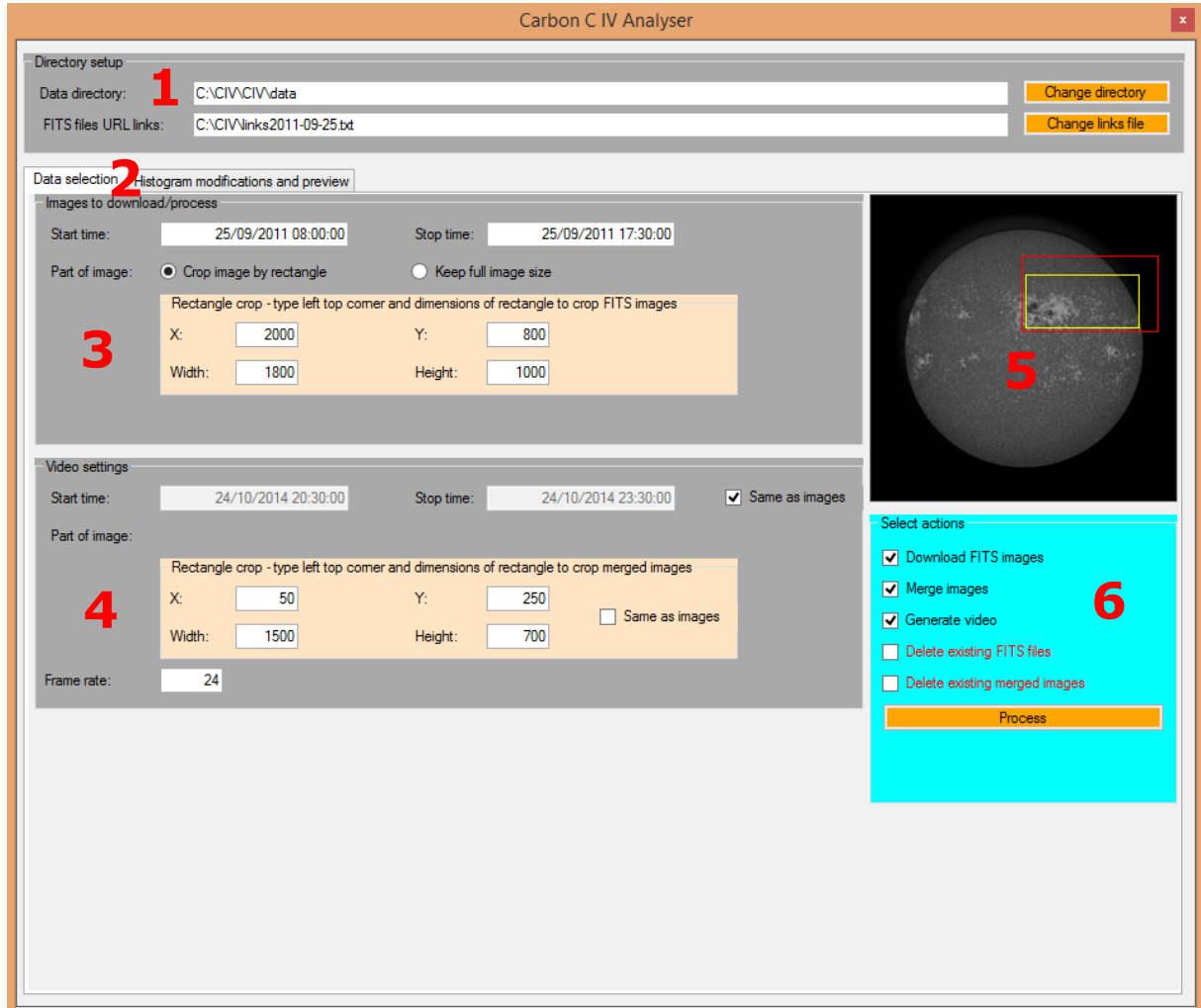


Figure 3.16: Graphical user interface with displayed tab *Data Selection*.

3.4.1 Data Selection tab

When *Data selection* is chosen, you can see similar layout as in the figure 3.16.

On top of tab *Data selection* there is a section {3} called *Images to download/process*, where you can set up time range of images to be downloaded or merged and decide whether you want to merge whole images or just its selected rectangular part.

Similarly in section {4}, you can specify time range and part of images to be included in the video. Be aware of the fact, that the rectangular part is selected with respect to already merged images and its dimensions. You have a possibility to select *Same as images* to keep same time range (and same rectangular part of image respectively) as for merged images. Also, you can specify the frame rate of video and influence 'speed' of an event.

In section {5}, there is a thumbnail of selected FITS image with marked merge images rectangle (the bigger red one) and video images rectangle (the smaller yellow one). Rectangles are updated each time, when some of rectangles' parameter is changed with feasible value. To be able to see thumbnail, first you have to select particular FITS images (see subsection 3.4.2 below).

Last part *Select actions* {6} allows to choose desired actions you want to run. You can download FITS files given by *FITS files URL links* in section {1} and time range in section {3}. Similarly, another option is to merge images of both wavelengths from already existing FITS files within given time range in section {1}. The third option is to generate video from already merged files with parameters given in section {4}. Multiple options might be selected to perform more tasks in single run. Last two options allow you to either clear all files in directories or continue in processing where you ended last time.

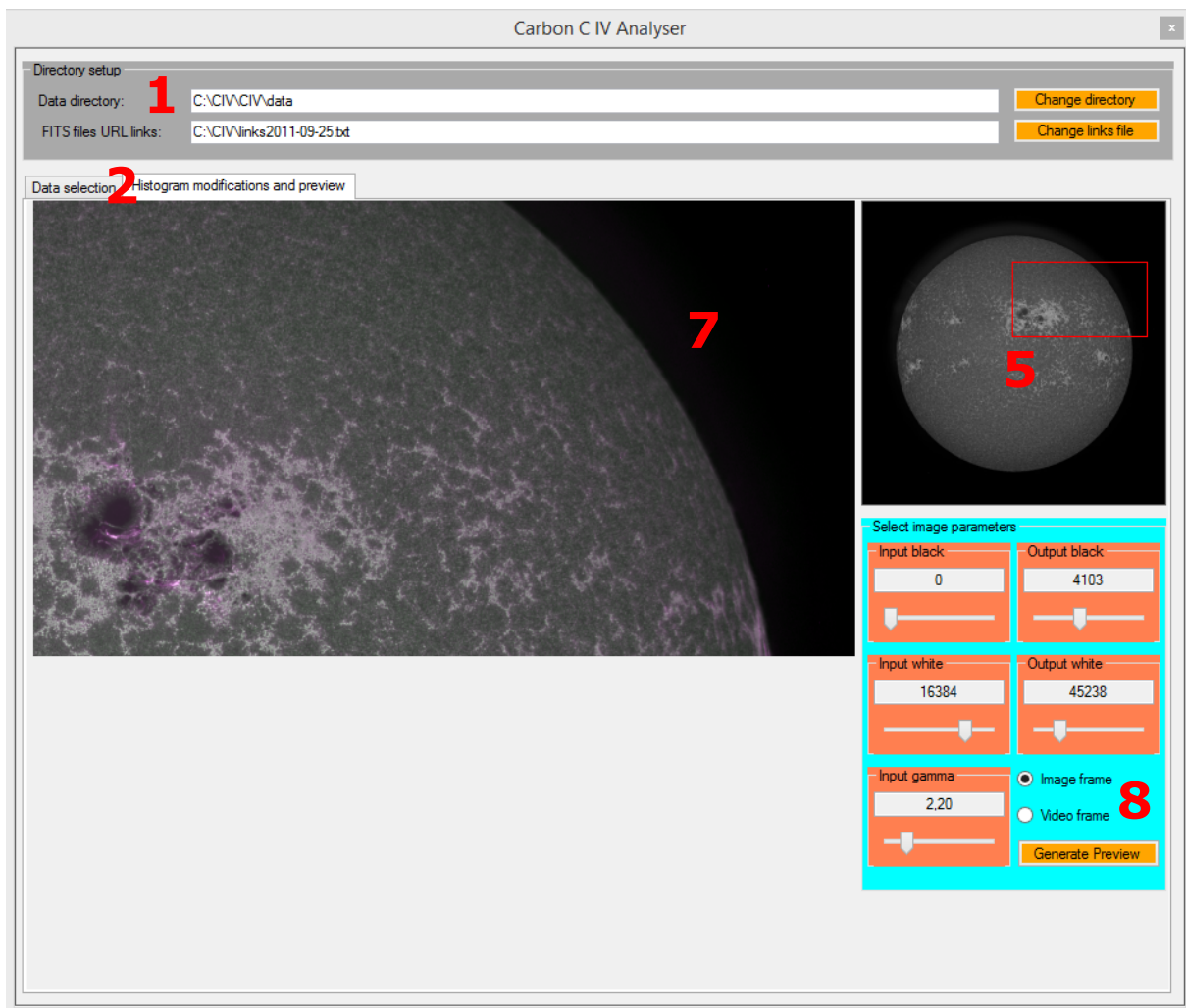


Figure 3.17: Graphical user interface with displayed tab *Histogram Modification & Preview*.

3.4.2 Histogram Modifications and Preview tab

When *Histogram modifications and preview* tab is chosen, you can see a similar layout as in the figure 3.17.

Again, there is a thumbnail section {5} and detail preview {7}. To see it, first you have to click on button *Generate preview* and select relevant 1600 Å FITS file and 1700 Å FITS file. Thumbnail {5} displays 1600 Å image, while the detail {7} displays merged images of both wavelengths with applied computed multiplicative function, gamma correction and linear transform respectively.

In section {8} called *Select image parameters* you can set up parameters *Input black*, *Input white* and *Input gamma* which correspond to a minimum pixel value, a maximum pixel value and gamma value respectively in used gamma correction (see subsection 2.3.2).

Furthermore parameters *Output black* and *Output white* correspond to minimum pixel value and maximum pixel value respectively in used linear transform (see subsection 2.3.1). Lastly, you can select whether you want to display the merged image or video image in detail section {7}.

Press of button *Generate preview* is required only once to select relevant FITS files, show thumbnail image and calculate detail image. Then the detail image is recalculated each time when any image parameter is changed.

3.4.3 Recommended usage and procedure

Before you launch the *Carbon C IV Analyser* for the first time, you may need to install Microsoft .NET Framework 4.5 or newer, if not already present on your computer. The installation file together with *Carbon C IV Analyser* is located in attachments. Maybe you will have to disable locally your anti-virus software and run program as administrator to achieve proper functioning. Also you can find in attached folder *Data_sample_2016-07-23_05-10_-_05-16* several FITS files which allow easy and fast testing images and video creation without slow download process. In folder *Eruptions* there is a couple of text files with links from interesting eruption and lastly, a couple of sample videos of eruptions are attached in folder *Videos*.

Now we will describe a short procedure on how to obtain a video of an eruption from scratch without requirement of any advanced knowledge of image processing techniques.

Once you decide which eruption you want to visualize, go to VSO, select all relevant files and export links to file. Change file extension to *.txt* and link it in *Carbon C IV Analyser* in section {1}.

In section {3}, select a short time range in the middle of the chosen eruption, just enough to involve at least one image from each wavelength and download it {6}.

Next, go to tab *Histogram modifications and preview* {2}, press *Generate preview* {8} and select downloaded FITS files from each wavelength.

After the preview and thumbnail is generated, go back to tab *Data selection* {2} and tune merge image rectangle parameters {3} to capture the place of an eruption. Back in tab *Histogram modifications and preview* tune image parameters until you are satisfied with displayed detail image.

Finally, select all actions {6} you want to perform and press *Process* button.

The most time consuming part of the complete process is to download FITS files due to limited downloading speed from VSO. Therefore if selected download and merge option together, both tasks are executed simultaneously. FITS files are downloaded in such an order that roughly corresponds to image couples to be merged and each such couple is merged immediately right after both files are downloaded.

Conclusion

Main objectives of the thesis have been fulfilled. In the first chapter 1, we have described the Sun regarding its atmosphere, how is it monitored by SDO, how often are data collected, in which way they are stored and how can it be obtained (see also subsection 2.1.1).

Further in chapter 2, the overall theory is summed up starting from a definition of an image, most often used image interpolation methods, histogram modifications and phase correlation. The couple of images was successfully registered by introduced phase correlation method with accuracy on tenths of pixels. The phase correlation method can be tuned up to be very robust for registering images capturing similar views (in our case the Sun disk). However, we were not looking for the best parameters setup, because we had a chance to register images using FITS headers. FITS headers contain keywords `RSUN`, `CROTA2`, `CRPIX1` and `CRPIX2`, which are sufficient to determine mutual transformation between our couple images (see subsection 3.1.3). This method was found to be more reliable without any tuning needed and also much faster, which is crucial when processing hundreds of large images couples.

After registration, we had to deal with different intensities of the continuum in both images (see subsection 3.1.4 and section 3.2). From all tested approaches we have got best results for the method of computing annuli medians of Sun disk with difference of diameters only 1 pixel. To achieve better results the medians were calculated by Kappa Sigma Clipping method (see subsection 2.3.3) and the medians at the midst of Sun disk were calculated for circle of radius 100 pixels to avoid low number of pixels involved in calculation. The ratio of corresponding medians from both images determined the designed multiplicative function to compensate continuum intensities in both images.

The calculation of multiplicative function is quite computationally and time demanding task. As exposure times are fixed, we should be able to use precomputed multiplicative function for multiple number of image couples. We have studied the usability of such a function in long term (see subsection 3.2.1). We have discovered inapplicability of such measures due to significant long term changes of multiplicative function caused by decrease of pixel intensities. Those are probably caused mainly by decreasing sensitivity of CCD chips of AIA.

Images were combined using color channels. The 1600 Å image with C IV was assigned to the red and blue component, while the 1700 Å image to the green one. Thus the resulting image was grey and the eventual presence of carbon C IV was highlighted by magenta color.

The resulting images suffered, due to high dynamical resolution, from low local contrasts in most parts of an image causing it to look dull. Only parts with C IV were high contrasting, sometime even suffered from blooming effect. Hence we needed image adjustment, this time from histogram point of view (see subsection 3.1.6). Firstly the gamma correction was applied. This helped to make the Sun disk brighter. But for contrast changes the saturation of an image was suggested. We can saturate the image as a whole. That gives a higher contrast in overall Sun disk but decreases or even destroys the contrast at highest intensities, namely at places with eruptions and C IV.

A videos were created of multiple image sequences capturing some major eruptions on Sun over the history of SDO observations. They can be found in attachments and also reproduced with different parameters thanks to created Graphical User Interface (see section 3.4).

This thesis provides a first glance in the visualisation of the Sun and its eruptions from the carbon C IV point of view. Further studies would be appropriate in many directions of mentioned topics.

For example, the evolution of pixel intensities and depending multiplicative function could be studied in more details to see if there can be found a simple dependence between average pixel values and its degradation in time or if there are perhaps more factors with measurable effects. For example, degradation of band pass filters could also have some influence.

Aside from saturation, another methods for making images more contrasting can be studied. For example there could be useful a histogram modification function designed in such a way, that it would stretch histograms around intensities of both histogram peaks and squeeze intensities between them. Apart from the global histogram modification approach, we could also try to use adaptive histograms methods, namely *A Noise Adaptive Fuzzy Equalization (NAFE)* [5].

Bibliography

- [1] BEZVODA, V., a kol. *Dvojměrná diskrétní Fourierova transformace a její použití - I.: Teorie a obecné užití*. 1. vydání. Praha: Státní pedagogické nakladatelství, n. p., 1988. 181 s. ISBN 17-135-88.
- [2] BASSILL. *SharpAvi* [online]. [cit. April 24, 2020]. September 3, 2019. <<https://github.com/baSSiLL/SharpAvi>>
- [3] BRIAN, N., *CSharpFITS* [online]. [cit. April 24, 2020]. April 2, 2016. <<https://github.com/SidWatch/CSharpFITS>>
- [4] *CURL: Command Line Tool and Library for Transferring Data with URLs* [online]. [cit. May 5, 2020]. <<https://curl.haxx.se/>>
- [5] DRUCKMÜLLER, Miloslav. *A NOISE ADAPTIVE FUZZY EQUALIZATION METHOD FOR PROCESSING SOLAR EXTREME ULTRAVIOLET IMAGES*. The Astrophysical Journal Supplement Series, 2013, vol. 207, issue 2, p. 25-29. DOI:10.1088/0067-0049/207/2/25.
- [6] DRUCKMÜLLER, M. *Numerické metody analýzy obrazů* (lecture). Vysoké učení technické v Brně, Fakulta strojního inženýrství, February 12, 2018.
- [7] DRUCKMÜLLER, M. *Numerické metody analýzy obrazů* (lecture). Vysoké učení technické v Brně, Fakulta strojního inženýrství, February 26, 2020.
- [8] DRUCKMÜLLEROVÁ, H. *Phase-correlation based image registration*, Brno, 2010. Diploma thesis. Vysoké učení technické v Brně, Fakulta strojního inženýrství. Supervisor Mgr. Jana Procházková, Ph.D.
- [9] FITS Working Group, *Definition of the Flexible Image Transport System (FITS)* [online]. [cit. December 1, 2019]. International Astronomical Union, August 13, 2018. <https://fits.gsfc.nasa.gov/standard40/fits_standard40aa-1e.pdf>
- [10] FOX, Karen C., *How SDO Sees the Sun* [online]. [cit. November 12, 2019]. Greenbelt, Maryland: NASA's Goddard Space Flight Center, 2017. <<https://www.nasa.gov/content/goddard/how-sdo-sees-the-sun>>
- [11] HOLČÍK, J.: *Signály, časové řady a lineární systémy*. 1. vydání. Brno: Akademické nakladatelství CERM, s.r.o., 2012. ISBN 978-80-7204-792-5.
- [12] HOWELL, E., *Solar Dynamics Observatory: Staring at the Sun* [online]. [cit. December 1, 2019]. July 13, 2018. <https://www.space.com/22081-solar-dynamics-observatory.html>
- [13] KARAS, P. *Studium metod registrace obrazu*. Brno, 2009. Diploma thesis. Masarykova univerzita, Přírodovědecká fakulta. Supervisor Mgr. Filip Hroch, Ph.D.
- [14] KOMRSKA, J. *Fourierovské metody v teorii difrakce a strukturní analýze*. 1. vydání. Brno: Vysoké učení technické v Brně, Nakladatelství VUTIUM, 2001. 222 s. ISBN 80-214-2011-1.

- [15] KOSOVÁ, P. *Numerical methods of space-based coronagraph image processing*, Brno, 2019. Diploma thesis. Vysoké učení technické v Brně, Fakulta strojního inženýrství. Supervisor prof. RNDr. Miloslav Druckmüller, CSc.
- [16] KOSOVÁ, P. *Parameter optimization of the modified phase correlation method for sub-pixel image registration*. Brno, 2017. Bachelor thesis. Vysoké učení technické v Brně, Fakulta strojního inženýrství. Supervisor Mgr. Jana Hoderová, Ph.D.
- [17] LEHMANN, Thomas M., GÖNNER, Claudia, SPITZER, Klaus. *Survey: Interpolation Methods in Medical Image Processing*. IEEE Transactions on Medical Imaging, vol. 18, issue 11, November 1999, p. 1049-1075, DOI:10.1109/42.816070.
- [18] LEMEN, J. R., TITLE, A. M., AKIN, D. J., BOERNER, P. F., CHOU, C., DRAKE, J. F., ... WALTHAM, N. *The Atmospheric Imaging Assembly (AIA) on the Solar Dynamics Observatory (SDO)*. Solar Physics, 2011, 275(1-2), p. 17–40. DOI:10.1007/s11207-011-9776-8.
- [19] Lumen Learning. *The Structure and Composition of the Sun* [online]. [cit. February 19, 2020]. <https://courses.lumenlearning.com/astronomy/chapter/the-structure-and-composition-of-the-sun/>
- [20] MEDUŇA, T. *Detekce otočení a změny měřítka obrazu užitím fázové korelace*. Brno, 2018. Bachelor thesis. Vysoké učení technické v Brně, Fakulta strojního inženýrství. Supervisor Mgr. Jana Hoderová, Ph.D.
- [21] MINTĚL, T. *Interpolace obrazových bodů*. Brno, 2009. Diploma thesis. Vysoké učení technické v Brně, Fakulta informačních technologií. Supervisor Ing. Michal Španěl.
- [22] NASA Goddard Space Flight Center. *Virtual Solar Observatory* [online]. <<https://sdac.virtualsolar.org/cgi/search>>
- [23] Newport Corporation. *Tutorial: Introduction to Solar Radiation* [online]. [cit. March 26, 2020]. 2020. <https://www.newport.com/t/introduction-to-solar-radiation>
- [24] NIGHTINGALE, R. W. *AIA/SDO FITS Keywords* [online]. [cit. February 13, 2020]. Joint Science Operations Center, October 20, 2010. <https://jsoc.stanford.edu/~jsoc/keywords/AIA/AIA02840_K_AIA-SDO_FITS_Keyword_Document.pdf>
- [25] PRATT, William K. *Digital Image Processing*. Hoboken, New Jersey: WILEY, 2007, ISBN: 978-0-471-76777-0.
- [26] SpacePlace. *Sunspots and Solar Flares* [online]. [cit. February 19, 2020]. NASA, September 12, 2019. <<https://spaceplace.nasa.gov/solar-activity/en/>>
- [27] *The FITS Support Office at NASA/GSFC* [online]. [cit. December 1, 2019]. Responsible NASA representative: Dr. Thomas A. McGlynn: High Energy Astrophysics Science Archive Research Center, 2017. <<https://fits.gsfc.nasa.gov/>>
- [28] University Corporation for Atmospheric Research. *"Parts" of the Sun* [online]. [cit. February 19, 2020]. UCAR, 2012. <<https://scied.ucar.edu/sun-regions>>
- [29] ŽÁRA, J., BENEŠ, B., SOCHOR, J., FELKEL, P. *Moderní počítačová grafika*. Brno: Computer Press, 2004. ISBN 80-251-0454-0.

List of abbreviations

AIA	Atmospheric Imaging Assembly, the instrument aboard space probe Solar Dynamics Observatory (see section 1.2)
ASCII	American Standard Code for Information Interchange, code table defining characters of English alphabet and other symbols used in informatics
CCD	Charged-coupled device, type of sensor for detecting and measuring light intensity
curl	Client URL, a command-line tool for transferring data using various network protocols
C IV	Three times ionized atom of carbon
DFT	Discrete Fourier transform (see definition 2.9)
EVE	Extreme Ultraviolet Experiment, the instrument aboard space probe Solar Dynamics Observatory (see section 1.2)
FITS	Flexible Image Transport System, format for storing and sharing astronomical data (see subsection 2.1.1)
FT	Fourier transform (see definition 2.6)
GUI	Graphical User Interface
HDU	Header/Data Unit, the structure of FITS files (see subsection 2.1.1)
HMI	Helioseismic Magnetic Imager, the instrument aboard space probe Solar Dynamics Observatory (see section 1.2)
IDFT	Inverse discrete Fourier transform (see definition 2.10)
IFT	Inverse Fourier transform (see definition 2.7)
NAFE	Noise Adaptive Fuzzy Equalization, adaptive histogram modification method [5]
px	pixel
RGB	red-green-blue color system
SDO	NASA's space probe Solar Dynamics Observatory (see section 1.2)
VSO	Virtual Solar Observatory, tool for searching and obtaining NASA's observation data (see subsection 1.2.1)

List of appendices

A Carbon C IV Analyser

B *Data_sample_2016-07-23_05-10_-_05-18* folder with sample FITS files

C *Eruptions* folder with links files of several eruptions

D *Videos* folder with created videos of eruptions